

## Study of polar thin ice clouds and aerosols seen by CloudSat and CALIPSO during midwinter 2007

Patrick Grenier,<sup>1</sup> Jean-Pierre Blanchet,<sup>1</sup> and Rodrigo Muñoz-Alpizar<sup>1</sup>

Received 31 July 2008; revised 15 December 2008; accepted 23 January 2009; published 1 May 2009.

[1] Data sets from CloudSat radar reflectivity and CALIPSO lidar backscattering measurements provide a new regard on Arctic and Antarctic winter cloud systems, as well as on the way aerosols determine their formation and evolution. Especially, links between the cloud ice crystal size and the surrounding aerosol field may be further investigated. In this study, the satellite observations are used to heuristically separate polar thin ice clouds into two crystal size categories, and an aerosol index based on the attenuated backscattering and color ratio of the sampled volumes is used for identifying haze in cloud-free regions. Statistics from 386 Arctic satellite overpasses during January 2007 and from 379 overpasses over Antarctica during July 2007 reveal that sectors with the highest proportion of thin ice clouds having large ice crystals at their top are those for which the aerosol index is highest. Moreover, a weak but significant correlation between the cloud top ice effective radius and the above-cloud aerosol index suggests that more polluted clouds tend to have higher ice effective radius, in 10 of the 11 sectors investigated. These results are interpreted in terms of a sulphate-induced freezing inhibition effect.

**Citation:** Grenier, P., J.-P. Blanchet, and R. Muñoz-Alpizar (2009), Study of polar thin ice clouds and aerosols seen by CloudSat and CALIPSO during midwinter 2007, *J. Geophys. Res.*, *114*, D09201, doi:10.1029/2008JD010927.

### 1. Introduction

[2] Owing to the paucity of scientific observations, clouds in the polar regions are poorly known relative to those at lower latitudes, and this contributes to the large range of uncertainties in present-day and future simulations of the polar climates [*Intergovernmental Panel on Climate Change*, 2007]. The lack of knowledge about clouds is particularly acute during dark months, in part because visual observations are difficult, but also because satellite infrared passive measurements cannot easily discriminate between cloud top and surface emissions, mainly owing to the frequent low-level temperature inversions [*Serreze and Barry*, 2005]. Therefore, cloud climatology varies largely among sources. *Curry et al.* [1996] have reviewed several of them to conclude that the mean cloud fraction ranges broadly between 40 and 68% during the Arctic winter, increasing to 80% if the generally unreported clear-sky ice crystal precipitation (diamond dust) is taken into account. They also mention regional disparities, the lowest wintertime cloud cover being over the Canadian Arctic and the highest over West Eurasia. Over Antarctica, cloud climatology is also highly variable among authors, for similar reasons. For the latitude bands between 65°S and 80°S during the period 1982–1991, *Hahn et al.* [1995] have computed a mean wintertime cloud cover ranging from 78 to 85% over the ocean (from ship observations) and from 47

to 69% over land stations, with values increasing equatorward. Again, these values could be higher if diamond dust was included. *Walden et al.* [2003] reported a 91% frequency of occurrence of these slowly precipitating crystals during 6 winters at the South Pole. Other properties, like regional distribution, base and top heights, particulate phase and concentration, ice effective radius and droplet size, also need more study for evaluation of the role of polar clouds in the atmospheric energy balance.

[3] Limited knowledge of the processes determining microphysical properties of clouds also hinders their proper simulation by numerical models. In particular, the interaction of the atmospheric water content with the aerosol field consists of a myriad of mechanisms, and it is not clear which of them dominate in cloud systems. During the Arctic polar night, sulphates represent an important aerosol species in terms of their impact on clouds, due notably to their high mass fraction in the total aerosol, their hydrophilic property and their ability to inhibit ice nucleation. *Christensen* [1997] estimated that European and Russian sources account for about 90% of anthropogenic sulphates injected into the Arctic air mass north of 75°N, but the proportion coming from Southeastern Asia has probably increased since the publication of his study, owing to an enhanced industrial activity. Also, contributions from the European and North American sources may vary with the prevalent circulation associated with the NAO phases [*Eckhardt et al.*, 2003]. In terms of concentrations, a decrease has been observed at the surface from the early 1990s until at least 2003 [*Sirois and Barrie*, 1999; *Quinn et al.*, 2007], owing to SO<sub>2</sub> emission control in Europe and to the collapse of the Russian economy at the beginning of this period. So, at first

<sup>1</sup>Institut des Sciences de l'Environnement, Université du Québec à Montréal, Montreal, Quebec, Canada.

approximation, it is most possible that radiative indirect effects induced by sulphates have decreased in strength during the last 20 years over the Arctic as a whole. However, in terms of sulphate-to-aerosol mass ratio, the decrease within the Arctic haze could be less pronounced, because of a decline in the concentration of some other pollutants, like black carbon [Sharma *et al.*, 2004]. Therefore, it is also possible that some indirect effects linked to the aerosol acidity (instead of the sulphate absolute concentration) have kept sustained strength during this period, and even increased over some sectors. Over Antarctica, the aerosol is also very acidic during winter, owing to the presence of sulphates which originate mostly from biological processes in the surrounding oceans [Shaw, 1988]. However, sulphate absolute concentrations are much lower than in the Arctic, and haze episodes are rare. Trends in the polar aerosol composition influence the cloud cover, which in turn influences the radiative budget and surface temperatures [Liu *et al.*, 2008].

[4] One particular property of the aerosol field which impacts on cloud properties is the concentration of ice forming nuclei (IFN). Observations by Borys [1989] indicate that the IFN concentration may be reduced by 1 to 3 orders of magnitude during Arctic haze events. These field measurements are consistent with the sulphate aerosol acting as an ice nucleation inhibitor, and we refer to this interaction as the sulphate-induced freezing inhibition (SIFI) effect. Unfortunately, laboratory results do not currently allow for a full understanding of this phenomenon, because of the great variety in the aerosol composition and size, as well as in the thermodynamic state. For example, Knopf and Koop [2006] have conducted experiments which show that the (heterogeneous) ice nucleation on some mineral dust particles is not significantly affected by H<sub>2</sub>SO<sub>4</sub> (sulphuric acid) coating, in a temperature range relevant for the Arctic troposphere. However, other results by Archuleta *et al.* [2005] show that for a lower temperature interval and different mineral dust compounds, sulphuric acid may considerably shift the supersaturation (and hence the temperature) required for ice nucleation to occur, toward lower or higher values. (NH<sub>4</sub>)<sub>2</sub>SO<sub>4</sub> (ammonium sulphate) coating may also affect the ability to nucleate ice [Eastwood *et al.*, 2008]. So, recent laboratory results as a whole neither directly support nor invalidate the SIFI hypothesis, and more data are needed for connecting field observations by Borys [1989] to laboratory experiments.

[5] Recently, Prenni *et al.* [2007] have demonstrated the important role of IFN concentrations in Arctic mixed-phase cloud model representations, and emphasized that their parameterization for the Arctic environment should differ from that for midlatitudes. Consistently, Blanchet and Girard [1994] and Blanchet [1995] have argued that the SIFI effect favors large ice crystal populations in the boundary layer, like diamond dust, at the expense of non-precipitating ice clouds or ice fog. Numerical simulations by Girard *et al.* [2005] have demonstrated that the SIFI effect triggers an important indirect climate effect in which clouds, precipitation and longwave radiation interact. Their simulations show that this process, called dehydration-greenhouse feedback (DGF), causes a strengthening of the surface temperature inversions by several degrees during Arctic haze events, because larger ice crystals in air masses

entering the Arctic are associated with a higher dehydration efficiency and with a lower water vapor greenhouse effect, whereas subsequent cooling feeds back into further dehydration. The DGF is most effective in the Arctic during winter, owing to a particular temperature regime. As temperatures decrease below about  $-30^{\circ}\text{C}$ , the Planck function shifts toward the water vapor rotation band in the far infrared, while the transmittance increases rapidly above  $17\ \mu\text{m}$  (in the so-called “dirty window”) with lowering water vapor concentrations. Because sulphuric acid coating of natural IFN is likely limiting freezing in the same temperature range, the DGF may represent an efficient climate-altering process. Possibly, the DGF is the strongest indirect effect of aerosols on climate, at least on a regional and seasonal basis. So far, this process was thought to be significant mostly in the boundary layer, but recently, with CloudSat and CALIPSO measurements, we found that a similar mechanism could take place higher in the Arctic troposphere.

[6] In this study, satellite measurements are used to investigate where the SIFI effect could be most significant during the polar dark months, and to what extent it may affect the size of ice crystals in light precipitation. We analyze and compare clouds and aerosol distributions for winter conditions in 11 sectors of the Arctic and Antarctic regions. The paper starts with a brief description of the CALIPSO and CloudSat data sets used, and the classification algorithm is described subsequently. Next, statistical and correlational calculation results are presented, and implications for the SIFI effect and the DGF mechanism are discussed. A new cloud classification of thin ice clouds (TIC) relevant to polar climate studies is proposed.

## 2. Observational Data Sets

### 2.1. CALIPSO Data Set

[7] CALIPSO was launched on 28 April 2006 and joined the A-Train constellation on a heliosynchronous orbit at an altitude of 705 km. The CALIOP instrument (Cloud-Aerosol Lidar with Orthogonal Polarization) aboard the platform is probing the atmosphere with a Nd:YAG laser, which produces pulses of 110 mJ at 532 nm and 1064 nm. Pulses have a length of 20 ns ( $\sim 6.7\ \text{m}$ ). The satellite tangential speed of about  $7.5\ \text{km s}^{-1}$  and the lidar pulse repetition rate of 20.16 Hz allow for a sampling profile at every  $\sim 333\ \text{m}$  on the ground, whereas the footprint is  $\sim 70\ \text{m}$ , due to a beam divergence of  $100\ \mu\text{rad}$ . Data above 8.2 km are averaged with the 2 neighboring profiles for a resolution of 1 km, whereas above 20.2 km the resolution decreases to 1.667 m. In the vertical dimension, the 532-nm signal resolution is 30 m between  $-0.5$  and 8.2 km, 60 m between 8.2 and 20.2 km and lower above 20.2 km. Further technical details about the mission may be found in a document by Hostetler *et al.* [2006], and an early assessment of the initial performance of CALIOP has been documented by Winker *et al.* [2007].

[8] For this study, we used the total ( $\beta_{532}$ ) and perpendicular ( $\beta_{per}$ ) attenuated backscattering fields at 532 nm. The beam is sent polarized, and a depolarization beam splitter in the receiver allows for a measurement of the perpendicularly polarized component in the return signal. The polarization lidar technique [Sassen, 1991] has been

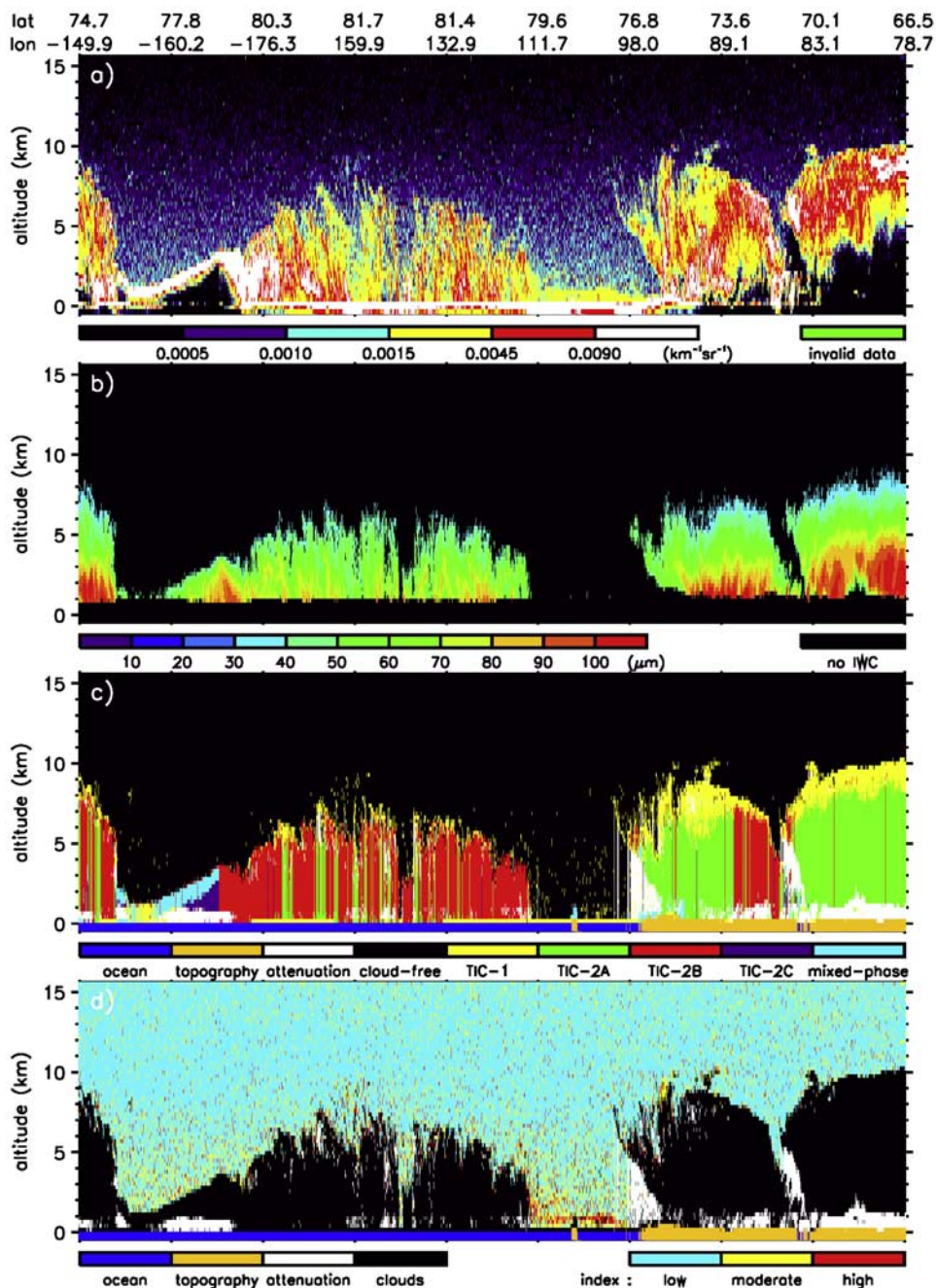


**Figure 1.** Fields from the selected Arctic scene: (a) measured  $\beta_{532}$  (CAL-LID-L1-Prov-V1-11.2007-01-19T21-36-47Z), (b) retrieved  $r_{ic}$  (2007019202553-03881-CS-2B-CWC-RO-GRANULE-P-R04-E02; black means  $r_{ic}$  is undefined), (c) cloud classification (data in first kilometer above the surface are invalid, but some bin flags have been filled by extrapolating the above feature, for presentation purpose only), and (d) aerosol index (low:  $\alpha \in [0,0.4[$ , moderate:  $\alpha \in [0.4,0.6[$ , high:  $\alpha \in [0.6,1]$ ).

applied for the detection of ice crystal layers, as explained later. We also used the total attenuated backscattering field at 1064 nm ( $\beta_{1064}$ ), for characterizing haze layers. Each measurement value (583 levels per profile) is georeferenced (latitude, longitude, altitude, along with time). In this study, we used the first version (V1) of the CALIPSO primary signals (data available in October 2007). Our conclusions may be modulated by newer data versions, but will not likely be fundamentally changed.

[9] Figures 1a and 2a show 4000-km-wide nighttime  $\beta_{532}$  transects over the Arctic (19 January 2007) and Antarctic (20 July 2007) regions, respectively. Horizontal resolution has been degraded to about 1100 m by averaging along-track and to 240 m in the vertical, for matching with the CloudSat products. It is intuitively expected that clouds, haze layers and clear air backscatter and absorb the lidar beam energy in decreasing orders of intensity. However, because this is plausibly only true in average, and because the beam gets strongly attenuated as it penetrates optically

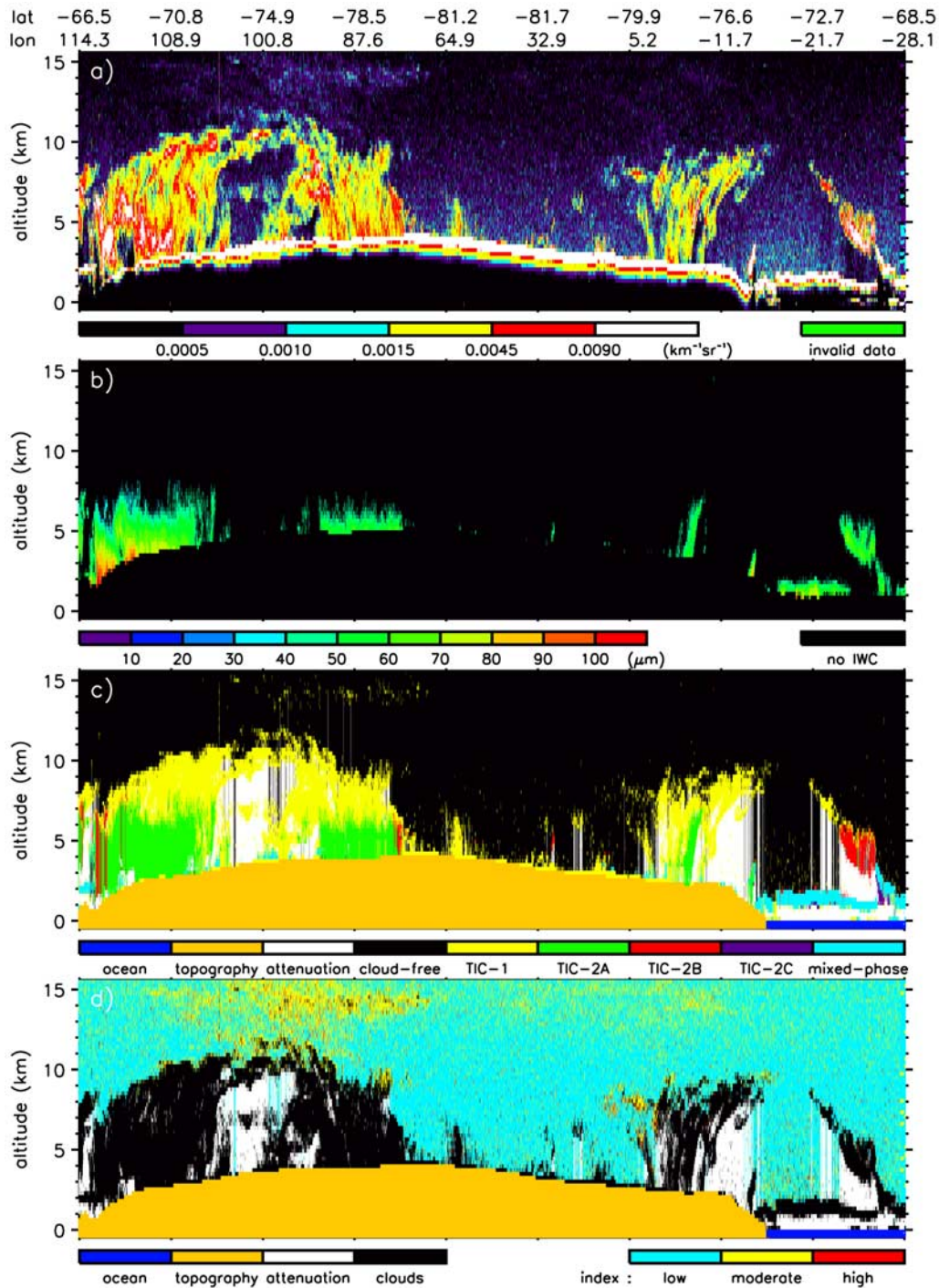


**Figure 2.** Fields from the selected Antarctic scene: (a) measured  $\beta_{532}$  (CAL-LID-L1-Prov-V1-20.2007-07-20T16-15-02ZN), (b) retrieved  $r_{ice}$  (2007201163104-06529-CS-2B-CWC-RO-GRANULE-P-R04-E02; black means  $r_{ice}$  is undefined), (c) cloud classification (data in first kilometer above the surface are invalid, but some bin flags have been filled by extrapolating the above feature, for presentation purpose only), and (d) aerosol index (low:  $\alpha \in [0,0.4[$ , moderate:  $\alpha \in [0.4,0.6[$ , high:  $\alpha \in [0.6,1[$ ).

dense features, complementary information is needed before assigning a feature tag (cloud, haze, or clear air) to each volume bin. Nevertheless, let us mention two interesting features that will be discussed later. The first is the boundary layer aerosol mass in the Arctic scene, between the tick marks at  $98.0^{\circ}\text{E}$  and  $111.7^{\circ}\text{E}$ . Inspection of ECMWF reanalysis (not shown) suggests that this haze event detected

by CALIPSO between the Taimyr Peninsula and the Bolchevik Island is occurring because a relatively high southward pressure gradient maintained along the Eurasian northern coasts during the previous days has transported pollution from Norilsk and/or the Kola Peninsula, but a numerical trajectory analysis is necessary to determine with more precision the origin of this polluted air mass. The

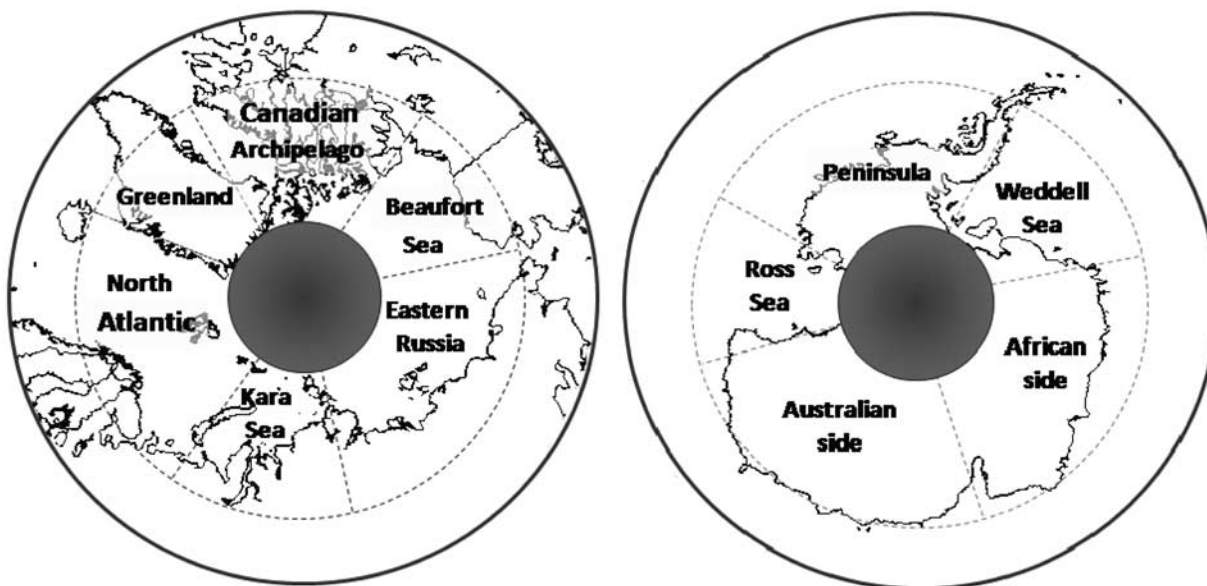


**Figure 3.** Sectors under investigation for January 2007 (Arctic) and July 2007 (Antarctica).

transport of aerosol from Eurasia into the Arctic during January 2007 is discussed by R. Muñoz-Alpizar et al. (The role of arctic cold lows in generating thin ice clouds: A comparison between CloudSat-CALIPSO and NARCM simulations, manuscript in preparation, 2009). The second feature consists of the polar stratospheric clouds (PSCs) over Antarctica, above the altitude of 12 km and approximately between the tick marks at  $64.9^{\circ}\text{E}$  and  $108.9^{\circ}\text{E}$ . In the CALIPSO data set, this type of cloud is dominant in winter over the Antarctic continent, and seldom found at its antipode, at least below 15 km and during the winter month investigated for this study.

## 2.2. CloudSat Data Set

[10] CloudSat joined the A-Train orbit at the same time as CALIPSO, the latter lagging by about 15 s. Hence, measurements from both platforms are nearly coincident in space and time. The CloudSat payload instrument is the Cloud-Profiling Radar (CPR), with a frequency of 94 GHz (3 mm wavelength). A profile sampling is performed at every  $\sim 1100$  m on the ground, with a  $1.4 \times 2.5$  km footprint (cross track  $\times$  along track), whereas the vertical sampling is 240 m, performed at 125 levels. More technical details about the CloudSat mission are documented by Stephens et al. [2002].

[11] The CloudSat primary (or level 1B) product is the radar reflectivity, in  $\text{dBZ}_e$ . Retrieved microphysical properties include the ice effective radius ( $r_{ie}$ ) from the R04 2B-CWC product (level 2). We used this field in our cloud classification algorithm in place of level 1B, mostly because it is georeferenced. The level 2 retrieval algorithm (first version) has been formulated by Austin and Stephens [2001]. Because Kahn et al. [2007] have found that the radar sensitivity is greatly reduced in the first 3–4 levels above the surface, we excluded data in the first kilometer above the surface (about 4 levels) from the analysis. This surface contamination effect in boundary layer data results from the radar pulse length of 1000 m [Schutgens and Donovan, 2004]. The R04 ECMWF-AUX temperature

field, which consists of the ECMWF analysis interpolated at the CloudSat sampling positions, is also used.

[12] Figures 1b and 2b show the  $r_{ie}$  fields corresponding to the CALIPSO  $\beta_{532}$  scenes presented previously. It cannot be deduced from these images that the radar does not see the wide low-level aerosol layer in the Arctic scene, since data for the first kilometer above the surface are removed, but inspection of the corresponding primary field (radar reflectivity, not shown) reveals no salient feature in this region. Also, a 1- to 2-km-thick band of intense backscattering at the top of the 2 cloud systems in the first 1000 profiles (on the right) is not seen by the radar (in the primary field). In the Antarctic scene, about half of the cloud volume transected by the lidar beam is missed by the radar, and the PSCs are not captured at all (also in the level 1 signal). Our classification of ice clouds is based on these differences, as explained below.

## 2.3. Investigation Zones and Periods

[13] Although sulphate concentrations and acidity in the Arctic culminate in April [Sirois and Barrie, 1999], we believe that the SIFI effect could be most important in January, when temperatures are much colder. For this reason, we selected January and July (coldest month in Antarctica) of 2007 for starting our investigation, but other cold months also deserve study in regard of the SIFI effect. CloudSat and CALIPSO cross the Arctic 14 or 15 times a day, but there are a few orbits whose data were not available at the moment of doing the analysis. For January 2007, data from 386 nighttime orbits have been used, for a total of 1,417,289 profiles. For July 2007 over Antarctica, 1,673,900 profiles from 379 overpasses have been investigated. These data sets are hereinafter respectively referred to as ARC-386 and ANT-379. For some of the results presented later, subsets of 30 (Arctic) or 31 (Antarctica) granules (overpasses) have been used, and these are named ARC-030 and ANT-031.

[14] The regions beyond the polar circles are vast ( $\approx 21$  millions  $\text{km}^2$ ) and heterogeneous in terms of many param-

**Table 1.** Geographical Delimitations of Investigated Sectors, With the Number of Profiles Used for the Study, an Estimation of the Average Cloud Fractions (Free Atmosphere Below 15 km) and the Linear Correlation Coefficient Between TIC-2B Cloud Top  $r_{ic}$  and the Above-Cloud Aerosol Index<sup>a</sup>

| Sector                 | Delimitations | Profiles  | Cloud Fraction (%) | $r_{ic}-\alpha$ LCC |
|------------------------|---------------|-----------|--------------------|---------------------|
| Arctic (January 2007)  | 66.5°N–82°N   | 1,417,289 | 63–76              | 0.11                |
| Beaufort Sea           | 170°W–125°W   | 175,572   | 48–65              | 0.13                |
| Canadian Archipelago   | 125°W–60°W    | 249,528   | 49–66              | 0.15                |
| Greenland              | 60°W–20°W     | 157,371   | 67–76              | 0.09                |
| North Atlantic         | 20°W–55°E     | 297,906   | 77–86              | 0.12                |
| Kara Sea               | 55°E–100°E    | 179,804   | 68–81              | 0.09                |
| Eastern Russia         | 100°E–170°W   | 357,108   | 64–77              | 0.10                |
| Antarctica (July 2007) | 66.5°S–82°S   | 1,673,900 | 62–74              | 0.07                |
| Peninsula              | 150°W–60°W    | 409,203   | 68–81              | 0.08                |
| Weddell Sea            | 60°W–20°W     | 186,865   | 68–83              | 0.14                |
| African side           | 20°W–75°E     | 453,417   | 62–74              | 0.00                |
| Australian side        | 75°E–165°E    | 418,462   | 47–60              | 0.03                |
| Ross Sea               | 165°E–150°W   | 205,953   | 70–84              | 0.14                |

<sup>a</sup>Linear correlation coefficient, LCC; above-cloud aerosol index,  $\alpha$ . The margin of confidence (95%) in the last column ( $r_{ic}-\alpha$ ) is within  $\pm 0.01$ .

eters that can potentially affect cloud populations, so that we have partitioned the polar areas in our analysis. For example, the Greenland plateau consists of a singular orographic environment, whereas the North Atlantic open waters allow for a higher surface flux of water vapor, sensible heat and sea salt than usually found at their latitudes. Owing to the main circulation, meridional aerosol injection into the Arctic is also asymmetric, with higher values on the Eurasian side. Figure 3 shows our partitioning of the polar regions, with the exact delimitations and number of investigated profiles presented in Table 1. The last two columns of Table 1 are discussed later. Unless otherwise specified, all heights are given relative to the sea level.

### 3. Methodology

#### 3.1. Feature Classification Algorithm

[15] The superposition of quasi-synchronous and collocated CALIPSO and CloudSat fields reveals that the instruments have different perspectives on the atmosphere. Indeed, instruments are not sensitive to the same atmospheric constituents, and their respective beams may penetrate at different depths within dense features. The lidar, with a short wavelength, may reveal the presence of very tiny particles on its beam path, including the smallest ice crystals and most aerosol layers. The drawback to this sensitivity is the beam often losing most of its energy before reaching the surface. This frequent situation, that we term “saturation,” occurs when the lidar is probing optically thick layers. However, this is not a serious limitation here since our study focuses on thin clouds detected by the lidar and corresponding to optical depths less than about 3. The radar, by pulsing at a wavelength of 3 mm, cannot detect tiny particles constituting aerosol layers, as well as clouds that are made of crystals smaller than about 28–30  $\mu\text{m}$  (R. Austin, personal communication, 2008; this limit is not fixed and depends on the particle number concentration). For a more precise view of the hydrometeor detection capabilities of the radar, we refer to G. Mace (Level 2 GEOPROF Product Process Description and Interface Control Document Algorithm version 5.3, 2007, [www.cloudsat.cira.colostate.edu/dataICDlist.php?go=list&path=/2B-GEOPROF](http://www.cloudsat.cira.colostate.edu/dataICDlist.php?go=list&path=/2B-GEOPROF)) (hereinafter Mace, online algorithm, 2007).

[16] The fact that the radar misses the fraction of ice clouds made of small particles offers a basis for separating

clouds into two broad categories: those seen only by the lidar, made of small particles only, and those seen by both instruments, having large ice crystals. The former are termed thin ice clouds of type 1 (TIC-1), whereas the latter are designated as TIC-2, the type referring to the number of active instruments detecting the cloud. The TIC locations and frequencies of occurrence, along with the correlations of their optical properties with those of the surrounding aerosols, may provide evidence for the SIFI effect and clues on cloud processes in polar regions. Although the distinction between TIC-1 and TIC-2 is arbitrarily determined by the radar sensitivity, it conveniently separates suspended from precipitating clouds. Indeed, ice crystal populations having particles larger than 30  $\mu\text{m}$  have a higher probability of being precipitating than those for which the size distribution hardly reaches this threshold. However, this criterion is not perfect, and it is possible that some TIC-2 bins are not significantly precipitating. We are also interested in separating cases with slow ice crystal growth rate from those growing very fast to precipitation size, as such an “explosive mode” could be a signature of the SIFI effect in the atmosphere. For this purpose, TIC-2 are further divided into TIC-2A, TIC-2B and TIC-2C. TIC-2A consist of the vertical extension of slowly growing TIC-1 layers for which it is reasonable to think there is a sustained production of ice supersaturation. Within TIC-1/2A systems, a gradual transition between activation and precipitation sizes takes place. In contrast, TIC-2B are not overlaid by TIC-1, and this is consistent with explosive growth occurring in the formation zone at the cloud top. A third category of TIC-2 is often encountered in polar regions. It occurs at warmer temperatures ( $T > 39^\circ\text{C}$ ), in association with mixed-phase clouds. In the lower troposphere, below about 4 km altitude, liquid water clouds frequently form in air largely supersaturated with respect to ice (30 to 40%). Upon freezing, droplets also produce explosive growth of a few ice crystals that rapidly sediment below the liquid layer, resulting in crystals seen by both instruments. These features, labeled TIC-2C, are similar to TIC-2B but initiated from liquid phase, owing to warmer temperatures.

[17] The algorithm that we have designed for identifying TIC types in the CALIPSO/CloudSat data sets takes into account the numerical values of the  $\beta_{532}$  field, as well as the depolarization and color ratios. The algorithm also consid-

ers the ice water content (IWC) field retrieved from the radar reflectivity signal, but only to separate zero from nonzero IWC bins. The ice effective radius ( $r_{ie}$ ) value is used for statistical calculations, but not for classifying features. Our classification is heuristic in the sense that it allows for a tracking of a cloud type which, we have reasons to think, is particularly affected by the aerosol field (TIC-2B), without the need of developing a complex retrieval algorithm from the lidar fields. The next paragraphs provide a description of the classification algorithm.

[18] First, a smoothing filter is applied to CALIPSO backscattering fields, below 8.2 km, to get 60 m (vertical) and 1 km (horizontal) resolutions. The arithmetic averaging operation allows for a vertical continuity in the  $\beta_{532}$  field, which is necessary for using the same backscattering threshold when discriminating clouds from background aerosols below and above this height. However, a slight discontinuity at 8.2 km remains in the  $\beta_{per}$  and  $\beta_{1064}$  fields, which echoes in the depolarization and color ratios. Next, each CALIPSO profile is associated to the closest CloudSat profile, and the average of the 3 or 4 profiles associated to a same CloudSat profile is performed. The same operation is repeated for the vertical levels (with a resolution of 240 m for radar data), so that 12 or 16 lidar backscattering values are averaged and associated to 1 radar reflectivity value in the operation of mapping CALIPSO fields on the CloudSat grid. This procedure insures data compatibility, while strengthening the signal-to-noise ratio. Only levels below 15 km are kept for subsequent analysis. Data in the first 1000 m have been excluded from the TIC statistical calculations, because of the surface contamination problem in the radar, as mentioned before. Next, an analysis is performed to assign a tag to each bin (pixel). Tags may correspond to the following features: cloud-free (molecular and aerosol), TIC-1, TIC-2A, TIC-2B, TIC-2C, mixed-phase, and saturated signal, the latter being attributed to below-cloud regions in order to exclude from the subsequent aerosol field analysis bins whose backscattering fields could be biased by strong attenuation.

[19] One recurrent feature in the CALIPSO data set is a low-level, thin and highly reflecting layer with a well-defined top, easily confused with the surface. One can see an example of such a cover extending over about 400 km in Figure 1a, around the tick mark at  $-160.2^\circ\text{E}$ . On the basis of the characteristically low depolarization ratio of this kind of cloud cover, we believe that liquid droplets are present most of the time. Our algorithm detects it by using the sharp  $\beta_{532}$  vertical gradients at its top and base, and classifies it as a mixed-phase layer before finding the TICs. Mixed-phase layers are typically overlaid by a  $\beta_{532} \leq b_1 = 0.0015 \text{ km}^{-1} \text{ sr}^{-1}$  cloud-free region and reach a peak value of  $\beta_{532} \geq b_2 = 0.0090 \text{ km}^{-1} \text{ sr}^{-1}$  within about 1000–1250 m (4–5 CloudSat vertical bins) below the top.

[20] Next, a pixel is classified as a TIC-2 feature simply if the ice water content in the level 2 CloudSat product is nonzero, unless it has previously been identified as part of a mixed-phase layer. TIC-2 are further separated into TIC-2A if they are found below a sufficiently thick TIC-1 layer, into TIC-2C if they are located under a mixed-phase layer, and into TIC-2B otherwise. When performing the distinction between TIC-2A and TIC-2B, the algorithm seeks for a TIC-1 presence above in the current profile, but also in the

neighboring profiles, for minimizing the effect of holes in the TIC-1 cover. A minimum number of 12 TIC-1 pixels is required, corresponding to a 960-m-thick layer if they are equally partaken between the 3 profiles, and PSCs are masked during this procedure by requiring a minimal temperature of  $-78^\circ\text{C}$  for TIC-1 pixels to count. Nevertheless, the distinction may sometimes be erroneous, owing to the large diversity of cloud configurations.

[21] The most difficult step in classifying features is no doubt the separation between TIC-1 and aerosol layers, the latter being included in the cloud-free category. This difficulty was also encountered by *Vaughan et al.* [2005] when formulating a CALIPSO feature detection algorithm. The primary distinction between both features should be a lower average  $\beta_{532}$  value for aerosols, but we found that any fixed threshold leads to a high proportion of misclassifications that are obvious in regard of the visual structure of the field, especially at the edge of clouds. We then choose a relatively low threshold at  $\beta_{532, \text{min}} = 0.0009 \text{ km}^{-1} \text{ sr}^{-1}$ , which favors TIC-1 at the expense of aerosols, and relabeled the bins as cloud-free if they did satisfy at least one of three other criteria. The first of these subsequent criteria is based on the depolarization ratio, defined as  $\delta \equiv \beta_{per}/(\beta_{532} - \beta_{per})$ . A compilation of cloud  $\delta$  values by *Sassen* [1991] has led to the conclusion that ice clouds generally have  $\delta \geq 0.5$ , contrasting with liquid cloud values of  $\delta \cong 0$ . Small  $\delta$  values should also characterize aerosols. For example, *Ishii et al.* [1999] report an average value  $\delta \approx 1.34\%$  for Arctic haze during a 4-winter observational campaign at Eureka, Canada. However, as *Sassen* [1991] mentioned, the off-nadir angle should be at least  $\approx 2.5^\circ$  for uniformly oriented ice plates, potentially frequent in the Arctic, to reveal their depolarization property. So, because of the very small off-nadir angle of the CALIPSO laser beam ( $\approx 0.27^\circ$ ) during the months of January and July 2007, some ice crystal pixels could display low depolarization ratios. We then allowed pixels with small  $\delta$  values to register as clouds if they present relatively high backscattering values, by designing the following relation between the minimal depolarization ( $\delta_{\text{min}}$ ) and the backscattering values:

$$\delta_{\text{min}} = a_0 + a_1/\beta_{532}. \quad (1)$$

[22] A variety of coefficients have been tested, and it appears that  $a_0 = 10^{-2}$  and  $a_1 = 3 \cdot 10^{-5} \text{ km}^{-1} \text{ sr}^{-1}$  are suitable values. Physically,  $a_0$  represents the minimal depolarization value that a pixel must display in order to be registered as a cloud, whereas  $a_1$  determines the slope of the segregating curve in the  $\delta_{\text{min}}$  versus  $\beta_{532}^{-1}$  plot. The color ratio, defined as  $\chi \equiv \beta_{1064}/\beta_{532}$ , has also been used, since from visual inspection of many Arctic scenes it seems that clouds present a ratio of  $\chi \approx 1$ , whereas  $\chi \leq 0.5$  characterizes aerosol layers. On the basis of theoretical calculations from *Liu et al.* [2002], who have worked on the development of another CALIPSO scene classification algorithm, we adopted the threshold  $\chi_{\text{min}} = 0.54$  for TIC-1 not satisfying  $\beta_{532} \geq 0.0030 \text{ km}^{-1} \text{ sr}^{-1}$ , this last threshold reflecting our observation that practically no pixel above this backscattering value seems to be part of an aerosol layer. Finally, we used a clustering criterion, so that indi-

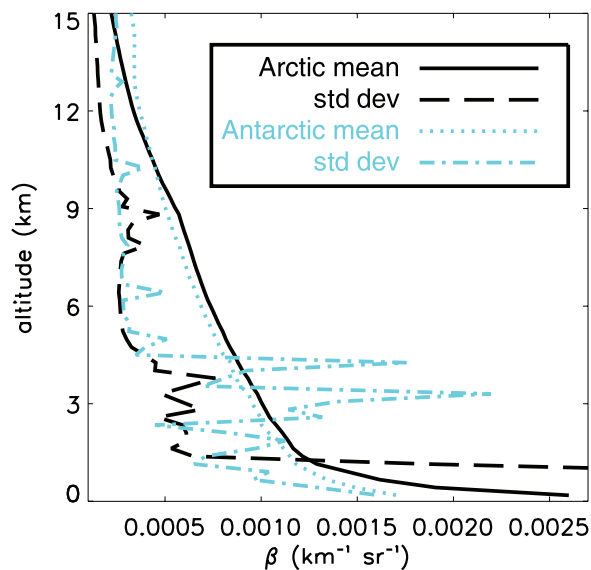


**Figure 4.** Mean cloud-free  $\beta_{532}$  profiles for the ARC-030 and ANT-031 subsets, with standard deviations.

vidual TIC-1 bins, resulting most often from noise, were reclassified as cloud-free.

[23] The temperature field, taken from the ECMWF reanalysis interpolated on the CloudSat grid (CloudSat ECMWF-AUX product), provides an ultimate criterion for determining the cloud phase. TIC pixels for which  $T \geq 0^\circ\text{C}$  are relabeled as mixed-phase layers (in principle it should be a liquid layer), whereas we considered that below  $-39^\circ\text{C}$ , the homogeneous freezing point, only ice clouds exist.

[24] Figures 1c and 2c illustrate how our algorithm classifies features seen by CALIPSO and CloudSat (same scenes as before). The first kilometer must be considered with caution since there is no radar data there. A mixed-phase layer is identified over the Beaufort Sea, but some parts of it are misclassified as TIC-1, owing to the absence of the steep  $\beta_{532}$  gradient at the base. The major part of the cloud system between tick marks  $-176.3^\circ\text{E}$  and  $111.7^\circ\text{E}$  (north of Laptev Sea) is classified as TIC-2B, with the exception of isolated profiles where there are enough TIC-1 pixels at the top for the algorithm to identify a TIC-2A feature. Extended on 1000 km over the Taimyr Peninsula, we see an important TIC-1 layer above a TIC-2A layer, divided in two systems. Some profiles are misclassified as TIC-2B often owing to holes in the TIC-1 cover, but most TIC-2B are correctly identified at the edge of one system. All pixels below significant cloud cover are considered lidar-saturated, and the rest is labeled as cloud-free. In the Antarctic scene, the major part of the system over the continent consists of a TIC-1/2A cover, and we see a small TIC-2B cloud formation and an extended mixed-phase cover over the Weddell Sea. PSCs are almost exclusively classified as cloud-free in this scene, but this is not always the case, these features being often partaken between TIC-1 and cloud-free, depending on their  $\beta_{532}$ ,  $\delta$  and  $\chi$  values. These results are fairly representative of the successes and limitations of the algorithm when applied to other winter

polar scenes of January and July 2007 (tests were performed on the 61 scenes of the ARC-030 and ANT-031 subsets to verify the feature classification results).

[25] As introduced before, we believe that TIC-2 populations differ in regard of their main growing processes. The microphysical distinction largely stems from synoptic-scale conditions. Indeed, synoptic systems possessing enough energy to raise air parcels as high as 9–10 km will also reach high ice supersaturation production rates and very likely activate a high proportion of the available ice-forming nuclei (IFN), either by deposition or contact mode. When supersaturation with respect to water is also reached, the condensation-freezing mode allows for even more IFN to be nucleated [Meyers *et al.*, 1992]. The small ice crystal populations thus formed (TIC-1) stay aloft longer, but precipitation will eventually be formed (TIC-2A). In contrast, when air parcels are slowly lifted, as is often occurring in the cold core of low-pressure systems in their cyclolysis phase, equilibrium between deposition and production of ice supersaturation may be reached, for which only large IFN whose acid coating is diluted enough nucleate into ice crystals, thus leading to less competition for water vapor. Ice crystal precipitation is then formed earlier (TIC-2B). TIC-2B may also be found at the edge of more active TIC-1/2A systems, where vertical motion and supersaturation production rate are weaker. The strength of the cooling rate, either from IR emission or adiabatic ascent, may be a key factor discriminating TIC types, since it reflects the production rate of ice supersaturation (but this is not used in this study).

### 3.2. Mean Cloud-Free Backscattering and Aerosol Index

[26] An important property of the CALIPSO  $\beta_{532}$  field is its mean cloud-free value, since this quantity can be an indicator of the concentration of aerosols in a sector. In fact, aerosols (as well as molecules) contained within cloudy bins also contribute to the measured backscattering. However, because it is extremely difficult, if not impossible, to properly separate their contribution from that of optically dominant liquid and ice particles, interstitial aerosols are not considered in our calculation of the mean cloud-free backscattering profiles presented in Figure 4 for the ARC-030 and ANT-031 subsets. One mean profile is presented for each polar region, along with the associated standard deviations ( $\sigma$ ). The granules contained in the subsets have been quasi-randomly selected, the only criteria being that each day be represented by at least one overpass (except when no data were available) and that transect orientations vary greatly, so that all sectors be represented many times. The high  $\sigma$  values at several levels, which are associated to cases where aerosols are difficult to distinguish from TIC-1, illustrate another limitation one faces when using an aerosol indicator based on the  $\beta_{532}$  information alone. In an attempt to minimize the impact of tenuous and misclassified TIC-1 layers on the aerosol signal, an aerosol index ( $\alpha$ ) which also considers the color ratio  $\chi$  ( $\equiv \beta_{1064}/\beta_{532}$ ) has been created and computed for each cloud-free pixel. It is defined as

$$\alpha \equiv \frac{w_\beta \cdot \min(\beta_{532}/2\beta_{ref}, 1) + w_\chi \cdot \max(0, 1 - \chi)}{w_\beta + w_\chi} \quad (2)$$

and varies from 0 to 1, with high values expected to reveal high pollution concentrations. Indeed, *Liu et al.* [2002] have computed from scattering models that mixtures of anthropogenic aerosols, typical of Arctic haze events, have lower color ratios than other natural aerosols like sea salt and dust particles, also found in the Arctic. This is related to size distributions, because smaller particles show lower  $\chi$  values, thus contributing to raise the aerosol index. Weights for the backscattering and color ratio terms were chosen so that  $w_\chi = w_\beta$ , whereas the backscattering reference value ( $\beta_{ref}$ ) varies with height and corresponds to the Arctic mean cloud-free backscattering profile presented in Figure 4. Aerosol indices for Antarctic pixels are also computed using the Arctic  $\beta_{ref}$  profile, for comparison against the same reference profile.

[27] The aerosol index fields obtained for the Arctic and Antarctic selected scenes are presented in Figures 1d and 2d. The part of the TIC-1 layer which is misclassified as cloud-free (Arctic scene, at  $\approx 9$  km, between tick marks 98.0°E and 89.1°E) shows a moderate index. If other parts of this TIC-1 cover are also misclassified as cloud-free, they show a low aerosol index due to a high  $\chi$  value. The low-level aerosol layer appears with a moderate or high aerosol index. In the Antarctic scene, the highly backscattering PSCs appear only with a moderate index, owing to their relatively high color ratio. Some zones around the continental TIC-1 system also exhibit a moderate aerosol index.

## 4. Results

### 4.1. Statistics on Clouds

[28] Figures 5 and 6 show the vertical distribution of the cloud type fractions for Arctic and Antarctic sectors, respectively. The fraction of a cloud type at a given level is calculated by dividing the number of bins for this type by the total number of profiles in the investigated zone (at this level). Results are presented between altitudes of 1 km and 15 km (68 levels). Vertical distributions contain no information on the overlap of cloudy bins, and hence on the “true” cloud fraction, defined as the percentage of sky that is covered with clouds at a single instant [*Intrieri et al.*, 2002], without regard of the height of the cloudy parcels.

[29] In the Arctic, TIC-1 (small crystal mode) are encountered preferentially over Greenland, North Atlantic and Kara Sea (hereinafter GNK) sectors, where they reach a maximum fraction near 0.23 at an altitude of  $\sim 8$ – $9$  km. The Eastern Russia, Beaufort Sea and Canadian Archipelago (hereinafter EBC) sectors are characterized by much lower TIC-1 peak fractions (0.06 to 0.14), also occurring at a lower altitude of  $\sim 7$ – $8$  km. Note, however, that the Eastern Russia sector contains more TIC-1 between 3 km and 6 km than any other sector. Consistently, TIC-2A fractions are higher in the GNK sectors, peaking at  $\sim 0.13$ – $0.14$  between altitudes of 4 and 6 km (indirectly shown on Figure 5a). The sum of the TIC-1 and TIC-2A curves suggests that the cyclone frequency is higher in these zones and/or that the convective activity is deeper. This is qualitatively consistent with the winter cyclone frequency climatology calculated by *Serreze and Barry* [2005] for the period 1970–1999, except for Greenland, where orographic lifting presumably contributes to cloud formation with little need from vorticity. Mixed-phase and underlying TIC-2C are also found

preferentially in the GNK sectors, with values between 1 and 2 km 3 to 4 times higher over North Atlantic than over EBC sectors (see Figure 5b). Figure 5c shows that the TIC-2B fractions are highest over Greenland and North Atlantic above 5 km, whereas Beaufort Sea and mostly Eastern Russia sectors have the highest fractions in the lower troposphere. When cloudy bins are summed up indistinctly of their type, vertical distributions (not shown) suggest that the clearest skies have occurred over the Beaufort Sea and Canadian Archipelago during January 2007, a condition which favors efficient longwave radiative cooling from the surface and lower levels. The Eastern Russian sector presents above-average overall cloudiness in the lower troposphere, because of the TIC-2B contribution. In terms of proportions, TIC-2B are most important for the Beaufort Sea, where they compose more than 50% of the cloud fraction below 5 km (Figure 5d). This proportion is also important for the Eastern Russia and Canadian Archipelago sectors, with more than 40% in the lower troposphere. GNK sectors present remarkably low TIC-2B proportions in the lower levels.

[30] As shown in Figure 6a, Antarctica is relatively similar to the GNK sectors in terms of small ice crystal and underlying TIC-2A vertical distributions. Especially, West Antarctica (Peninsula) has a TIC-1 + TIC-2A distribution very similar to that of Greenland. No Antarctic sector is as poor in TIC-1 + TIC-2A as the EBC sectors. Above an altitude of about 12 km, the contribution of PSCs to the TIC-1 distributions becomes clear, especially for the African portion of East Antarctica. West Antarctica appears markedly less covered by PSCs between 12 and 15 km than the other sectors, and as shown later this is not due to PSCs being flagged as aerosol. Figure 6b suggests that mixed-phase and underlying TIC-2C are as frequent over Antarctica as over the Arctic, but because of the height of the plateau, only the Ross Sea and Weddell Sea areas are well represented by the associated curves at low levels, whereas curves for the continental sectors correspond almost exclusively to their margins and the surrounding oceans. This representativeness issue is apparent from the discontinuities in the slope of East Antarctica sector curves 1 km above the average height of the plateau. Concerning TIC-2B, results indicate that they occur in similar fractions over all Antarctic sectors, but are 25 to 30% less frequent in the lower troposphere over the whole Antarctica than over the whole Arctic, owing to the strong contributions from EBC sectors. Above 6 km, results become similar. The sector-to-sector TIC-2B variability is also lower for Antarctica. In terms of proportions, TIC-2B account for roughly 20 to 35% of all clouds below 6 km, just like GNK sectors, and contrasting against EBC sectors.

### 4.2. Cloud Fraction

[31] From the scene classification, we can calculate the standard cloud fraction, defined as the fraction of profiles containing one or more cloudy bins, regardless of their height. Results are gathered in Table 1, in the form of intervals whose limits have been obtained by two different sets of thresholds. For the highest limit, we have used the results from the baseline algorithm, requiring for a profile that only one pixel be cloudy and using the threshold  $\beta_{532\_min} = 0.0009 \text{ km}^{-1} \text{ sr}^{-1}$ , whereas for the lower one,

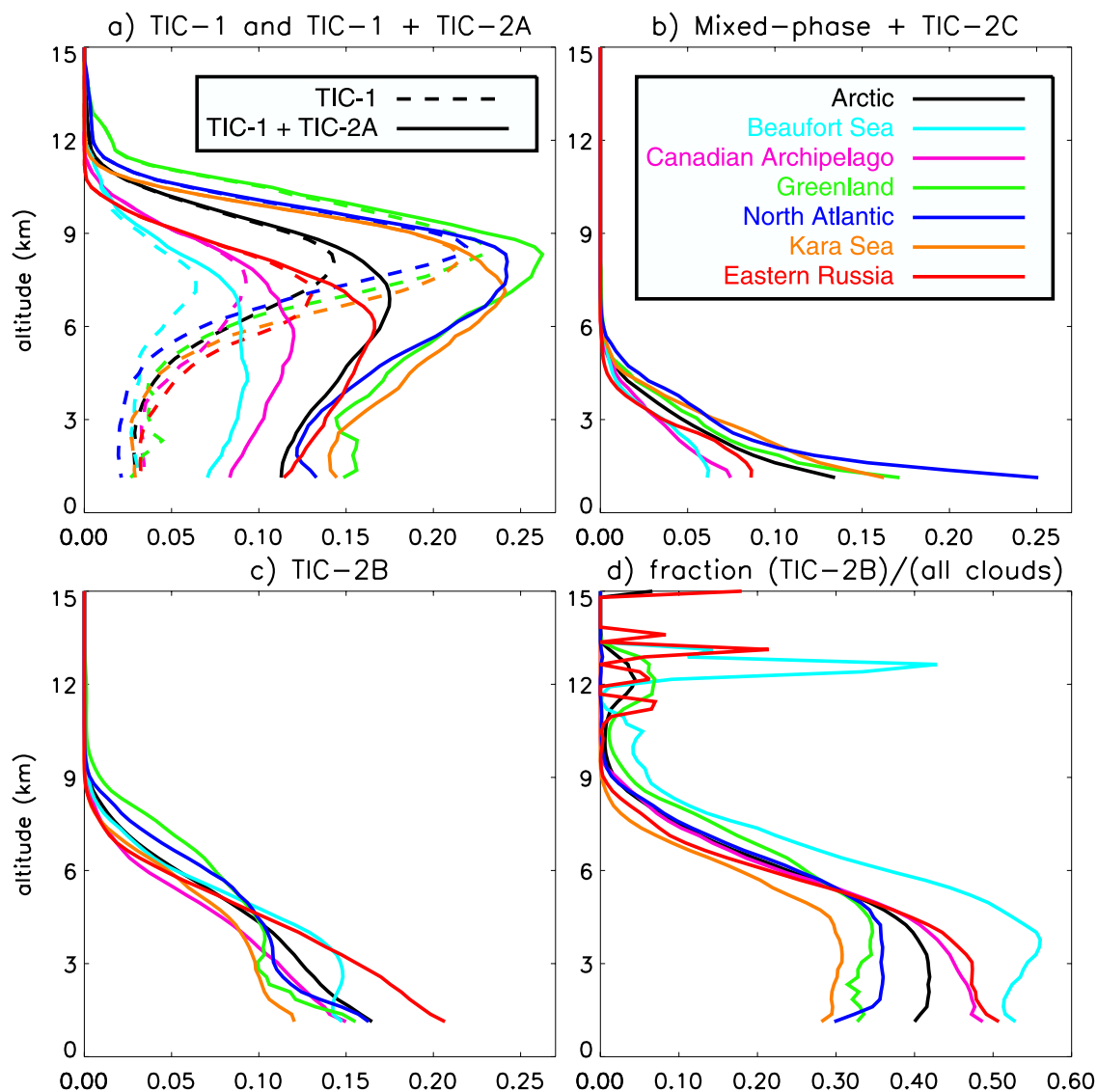


**Figure 5.** Vertical distribution of cloud fractions for Arctic sectors (see geographical delimitations in Table 1). Curves in Figures 5a, 5c, and 5d follow the same color code as in Figure 5b.

two cloudy bins were required, with a threshold increased to  $\beta_{532\_min} = 0.0012 \text{ km}^{-1} \text{ sr}^{-1}$ . For the investigated months, cloud cover estimates over the Arctic (63–76%) and Antarctica (62–74%) are similar. There is however variability within these broad regions. The Beaufort Sea (48–65%) and Canadian Archipelago (49–66%) sectors present the lowest estimates in the Arctic, whereas North Atlantic (77–86%) is the cloudiest of the 11 sectors. Over the southern continent, the Ross and Weddell Seas show the highest cloud fraction estimates, followed by West Antarctica, whereas the Australian Side of East Antarctica (47–60%) presents the lowest cloudiness of the 11 sectors. Unfortunately, these results say nothing about the latitudinal distribution of the cloud cover. Boundary layer (first kilometer above the surface) clouds have not been included, and PSCs above 15 km could increase values for Antarctic sectors, but only slightly since these usually form above other cloud systems. Visual inspection of the ANT-031 scenes below 15 km have clearly revealed PSCs in 29 of them, but no single scene contains PSCs in the ARC-030 subset.

#### 4.3. Statistics on Aerosol Properties

[32] The aerosol index ( $\alpha$ ) has been designed for emphasizing cloud-free volume bins which exhibit a high  $\beta_{532}$  and/or a low  $\chi$  value (equation (2)), characteristic of small sulphate particles in the nucleation mode, but maybe of other aerosol compounds as well. Mean profiles of  $\alpha$  calculated for January 2007 (Figure 7a) show that Eastern Russia and the Beaufort Sea have markedly higher aerosol concentrations than the Arctic average in the lower troposphere, whereas North Atlantic and Kara Sea have concentrations lower than the average. In January 2007, the Canadian Archipelago and Greenland are the sectors most representative of the Arctic-wide average in terms of the aerosol index, excepted for Greenland in the lower levels, where only the margins contribute to the statistics.

[33] Using the Northern Aerosol Regional Climate Model (NARCM) [Gong *et al.*, 2003], which explicitly simulates the fields of 5 aerosol species (sea salt, sulphates, black carbon, organic carbon and dust) segregated in 12 size bins, Muñoz-Alpizar *et al.* (manuscript in preparation, 2009) have

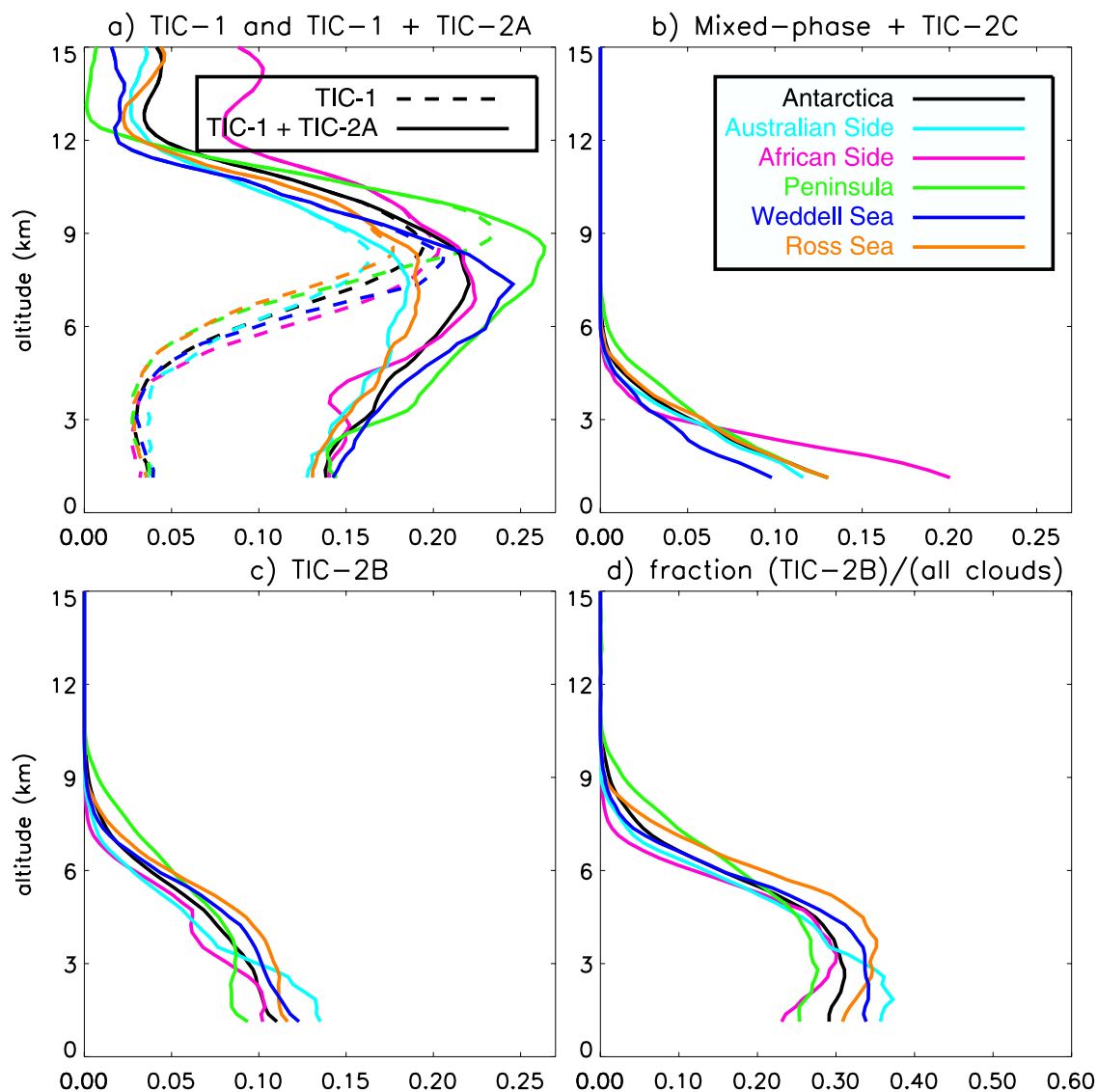


**Figure 6.** Vertical distribution of cloud fractions for Antarctic sectors (see geographical delimitations in Table 1). Curves in Figures 6a, 6c, and 6d follow the same color code as in Figure 6b.

shown that Eastern Russia and Beaufort Sea were the Arctic sectors in which the sulphate concentrations and the sulphate mass fraction in the total aerosol have been highest during January 2007. This suggests that high values of the aerosol index most likely occurred during sulphate-enriched haze events. Figure 7b shows that the threshold  $\alpha = 0.6$  in noncloudy bins is crossed most often over Eastern Russia and the Beaufort Sea. If we use this threshold for isolating haze from clean air, we obtain that for all Arctic sectors haze occurs most frequently between altitudes of 1000 and 1500 m, and for roughly about 8 to 15% of all noncloudy bins. Above 5–6 km, the relative contribution from noisy pixels having a very low color ratio becomes high. The jump at 8.2 km in the curves of Figure 7 is an artifact coming from the two-step averaging procedure of the  $\beta_{per}$  and  $\beta_{1064}$  fields, as discussed previously, and bears no physical meaning.

[34] Over Antarctica, the mean aerosol index and haze frequency of occurrence in noncloudy bins are much lower, and the variability among sectors is small (Figures 7c and 7d). Maximal haze occurrence occurs near 1000 m for all

sectors, but this cannot be true over the continental plateau (surface around 3000 m altitude). Peak values of  $\alpha$  are 2–3 times lower than over the Arctic. If we rely on the aerosol index as an occurrence criterion for anthropogenic aerosols (small and highly backscattering atmospheric constituents), we may conclude that during July 2007 over Antarctica, air masses were much less polluted than during January 2007 over the Arctic. This difference is due to the intensity and proximity to the Arctic of the Northern Hemisphere anthropogenic sources. The presence of PSCs is also revealed by the  $\alpha$  mean profiles, mostly over the African Side of East Antarctica and much less over West Antarctica (Peninsula). However, in most cases,  $\alpha = 0.6$  is a threshold too high for capturing PSCs.

#### 4.4. Color and Depolarization Ratios

[35] In this section, we discuss differences between cloud types and haze using scatterplots in the  $(\beta_{532}, \chi)$  and  $(\beta_{532}, \delta)$  spaces. We used profile bins of the ARC-030 subset below 8.2 km, and cloud-free bins are partitioned into haze

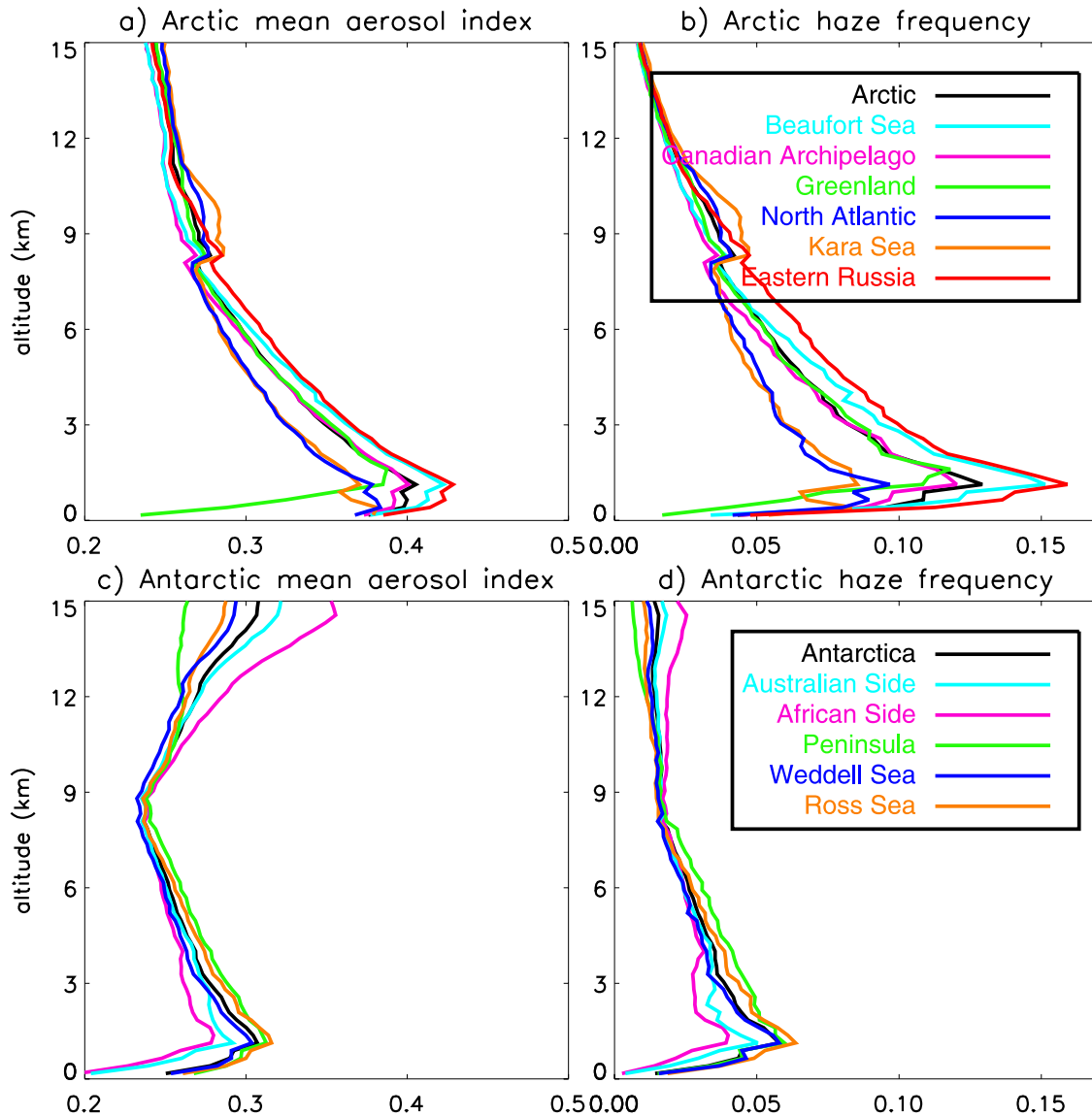


**Figure 7.** Vertical distribution of the Arctic (a) aerosol index fraction and (b) haze occurrence in cloud-free bins. Equivalent curves for the Antarctic (c) aerosol index fraction and (d) haze occurrence. Curves in Figure 7a follow the same color code as in Figure 7b, whereas curves in Figure 7c follow the same color code as in Figure 7d.

and molecular categories, with the requirement that haze satisfy  $\alpha \geq 0.6$ , corresponding to red zones in Figures 1d and 2d.

[36] Figure 8a shows the distribution of all bins in the  $(\beta_{532}, \chi)$  space. Scatterplots are also presented by feature categories. Molecular pixels (not shown individually) appear mostly below  $\beta_{532} \approx 0.0020 \text{ km}^{-1} \text{ sr}^{-1}$ , but a significant number of pixels are found above this value, along the  $\chi \approx 1$  line, owing to very low depolarization ratios which exclude them from the TIC-1 category, and to high color ratio values which subsequently exclude them from the haze category. A greater lidar off-nadir angle during measurements could have resulted in some of these pixels being classified as TIC-1, by avoiding low  $\delta$  reflections. Haze occupies a small region in the  $(\beta_{532}, \chi)$  scatterplot, corresponding to cloud-free pixels having at

the same time a high  $\beta_{532}/\beta_{ref}$  and a low  $\chi$  value. High color ratio bins ( $\chi > 2$ ) correspond to either low  $\alpha$  cloud-free pixels (molecular, with small signal-to-noise ratio) or lidar saturation layers. Bins for which the radar retrieval identifies ice clouds in the low  $\beta_{532}$  / high  $\chi$  region of the scatterplots correspond to the bottom parts of cloud systems, where the  $\beta_{532}$  field shows important attenuation. The fact that the maxima of occurrence of TIC-2A and TIC-2B bins (above  $\beta_{532} \approx 0.0010 \text{ km}^{-1} \text{ sr}^{-1}$ ) are found slightly below the  $\chi \approx 1$  line is consistent with the high  $\chi$  values associated to saturated signals, and means that the 1064 nm probing wave penetrates deeper in this kind of clouds. If a perfect retrieval of the volume backscattering fields was performed, these low  $\beta_{532}$  / high  $\chi$  TIC-2 bins would most probably move toward the TIC-2 maxima of occurrence. A huge fraction of mixed-phase bins are found for  $\beta_{532} > 0.0050 \text{ km}^{-1} \text{ sr}^{-1}$ , coarsely in

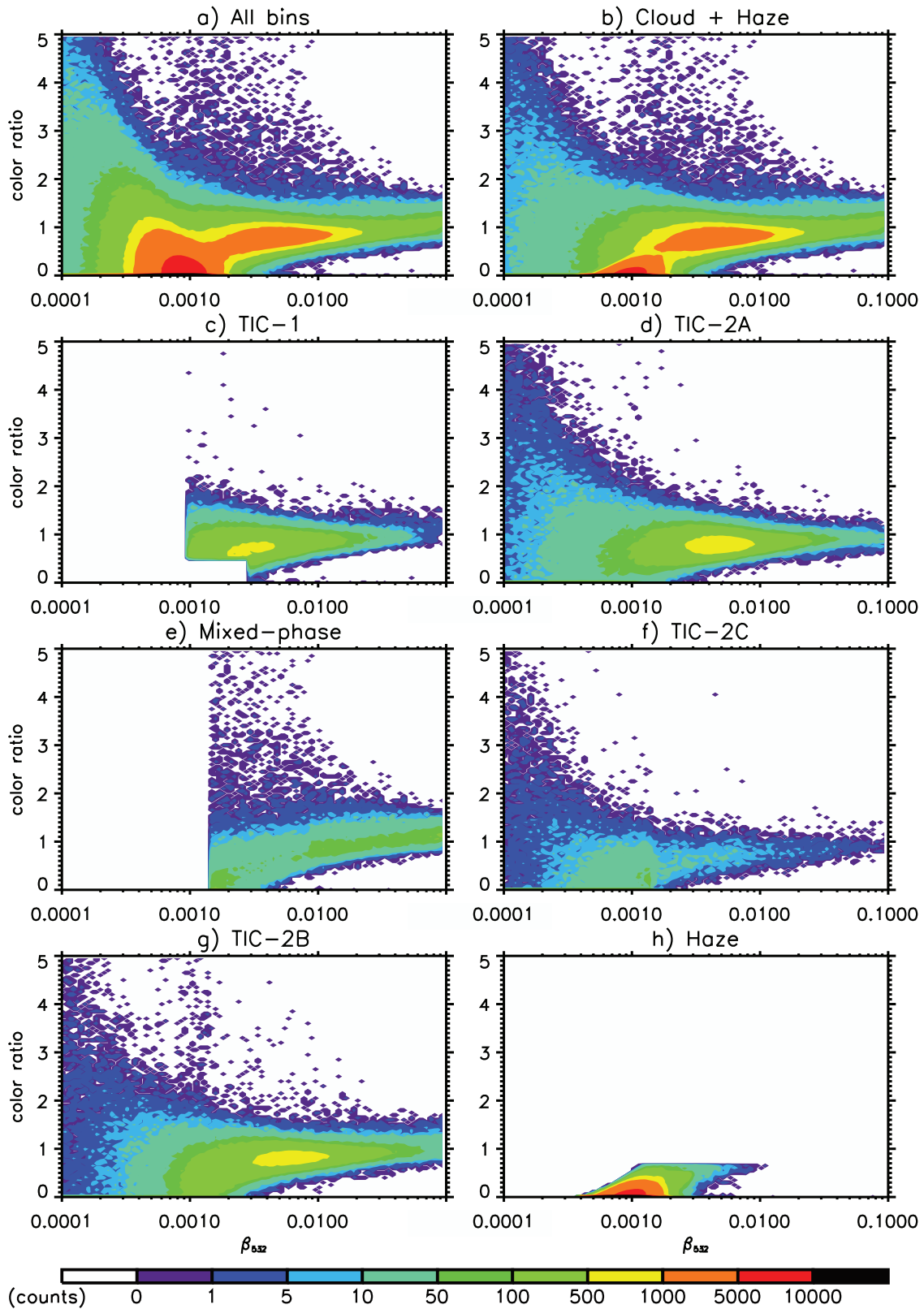


**Figure 8.** Scatterplots in the  $(\beta_{532}, \chi)$  space, for (a) all bins below 8.2 km of the ARC-030 subset, (b) cloud and haze, (c) TIC-1, (d) TIC-2A, (e) mixed-phase, (f) TIC-2C, (g) TIC-2B, and (h) haze bins.

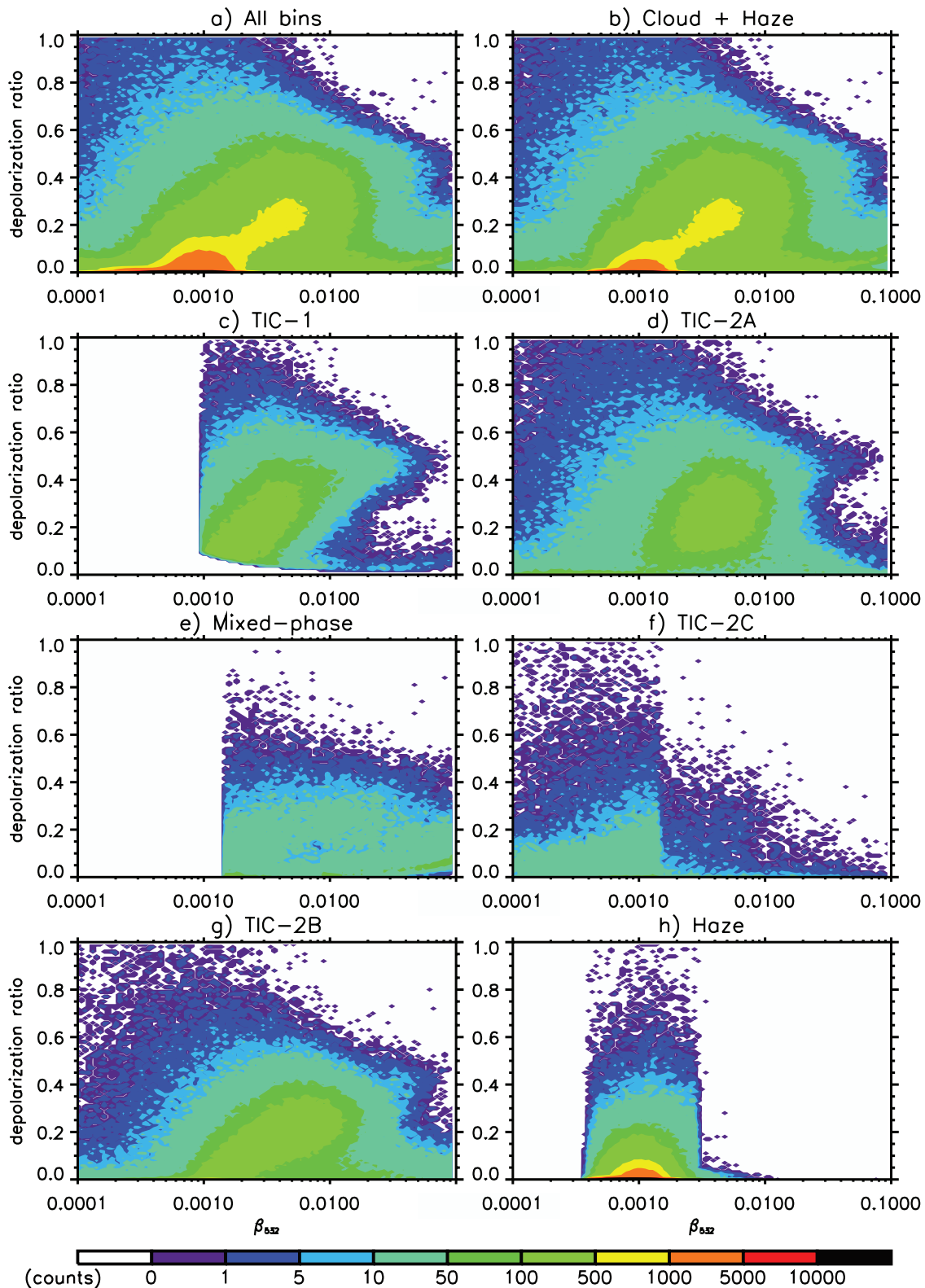


**Figure 9.** Scatterplots in the  $(\beta_{532}, \delta)$  space, for (a) all bins below 8.2 km of the ARC-030 subset, (b) cloud and haze, (c) TIC-1, (d) TIC-2A, (e) mixed-phase, (f) TIC-2C, (g) TIC-2B, and (h) haze bins.

the range  $\chi \in [0.6, 1.6]$ . However, mixed-phase clouds also present a distinct maximum of occurrence near the haze maximum. This suggests that some bins may have been misclassified and that the mixed-phase  $b_1 = 0.0015 \text{ km}^{-1}$

$\text{sr}^{-1}$  parameter (cutoff) could be increased. This would reclassify pixels at the top of these layers as haze, and those at the base as haze or saturated. This difficulty in clearly establishing the position of the layer top suggests a high sensitivity to the

$b_1$  parameter when calculating any correlation between mixed-phase layer properties and overlying aerosol indicators. In fact, all thresholds used for isolating features, most apparent in TIC-1, haze and mixed-phase ( $\beta_{532}$ ,  $\chi$ ) scatterplots, potentially have a significant effect on statistics and correlations presented in this study. This point is further discussed later.

[37] Figure 9 shows the ( $\beta_{532}$ ,  $\delta$ ) scatterplots for all bins and for individual feature categories. The high region of occurrence in Figure 9a, extending roughly from (0.0001, 0) to (0.0010, 0), includes mainly cloud-free and saturated bins, although some radar-seen bins, which correspond to the saturated zones in the bottom of TIC-2, are also located there. Out of the TIC-2A maximum of occurrence, the fact that the perpendicular fraction of the  $\beta_{532}$  returned signal increases as  $\beta_{532}$  shows more and more saturation may possibly indicate that crystals are less horizontally oriented in the bottom layers of TIC-2A. TIC-2A show a broad maximum around (0.0045, 0.25), but TIC-2B extend their maximal zone of occurrence to very low  $\delta$  values around  $\beta_{532} \approx 0.0010 \text{ km}^{-1} \text{ sr}^{-1}$ , coinciding with the haze maximum. Possible explanations are that the radar sees some wet giant particles like sea salt aggregates, or that some radar sampled volumes contain distinct ice crystal and aerosol regions. Departures from lidar and radar measurement collocation and synchronicity may also result in one instrument seeing clouds and the other seeing nearby haze, especially at TIC-2B tops. The fact that TIC-2A ( $\beta_{532}$ ,  $\delta$ ) scatterplots do not present the same maximum extension toward small  $\delta$  values is consistent with higher convective energy, which prevents crystals from horizontally orientating and promotes clustering of ice crystal aggregates. TIC-2A and TIC-2B patterns in ( $\beta_{532}$ ,  $\delta$ ) scatterplots show no threshold effect, since the mask for ice water content has been applied on the level 1B radar reflectivity field and not in our algorithm. This cutoff is variable, around  $-28$  or  $-30 \text{ dBZ}_e$  (Mace, online algorithm, 2007). TIC-1 bins extend their maximum of occurrence very close to the haze maximum, at about  $\beta_{532} \approx 0.0010 \text{ km}^{-1} \text{ sr}^{-1}$ , and this proximity is due to the small lidar off-nadir angle. Nevertheless, the exclusion of bins identified by the algorithm as molecular and saturated (Figure 9b) allows for a resolution of these maxima. High  $\delta$  bins in the haze distribution present low  $\chi$  and high  $\alpha$  values. Finally, mixed-phase clouds, whose identification is based on  $\beta_{532}$  vertical gradient considerations, preferentially show lower  $\delta$  values than TIC-2 do. Important departures from zero may be due to ice crystal contributions, and/or multiple scattering effects [Hu, 2007].

#### 4.5. Ice Effective Radius–Aerosol Index Correlation

[38] Calculations of the linear correlation coefficients (LCC) between retrieved  $r_{ie}$  values (CloudSat level 2 product) at the top of TIC-2B (3 upper bins) and the aerosol index of layers above (6 bins, TIC-1 excluded) have been performed. Results for the different sectors vary between 0.08 and 0.15, except for East Antarctica sectors which have lower values (see Table 1). All  $r_{ie} - \alpha$  LCC results have their 95% confidence interval within  $\pm 0.01$ , as obtained through Fischer's z-transformation test. Hence, results are significant for all sectors, except over the African side of Antarctica. However, results could be dependant on algo-

rithm parameters. The physical interpretation is discussed below.

## 5. Discussion

### 5.1. Implications for the SIFI Effect

[39] Analysis of CALIPSO and CloudSat data sets shows marked and very significant regional differences in the proportion of TIC-2B in the Arctic lower troposphere cloud cover during January 2007 (from  $\sim 30\%$  over Kara Sea to  $\sim 55\%$  over Beaufort Sea at 4500 m), but much less in the Antarctic cloud cover during July 2007 (between 25 and 35% at 4500 m). Regional variability is also observed in the lower troposphere frequency of haze occurrence over the Arctic (between 5 and 8% at 4500 m), but much less over Antarctica (between 3 and 4% at 4500 m). Moreover, Arctic sectors presenting lower troposphere TIC-2B proportions much higher than the average are the same for which haze occurrence is clearly above average, i.e., Eastern Russia and Beaufort Sea. The Canadian Archipelago also presents a high TIC-2B proportion, but a frequency of haze occurrence close to the Arctic average value. Other Arctic sectors and all Antarctic sectors present much lower (background) aerosol index values in the lower troposphere. An important question raised by the finding that TIC-2B proportions and outside-cloud pollution levels are high in the same sectors is whether haze aerosols are also found in great amount within TIC-2B systems. Short of in situ measurements for aerosol composition in TIC-2B, we performed numerical simulations with NARCM [Gong *et al.*, 2003] for assessing the concentration, size distribution and acid fraction of the Arctic aerosol during January 2007 (Muñoz-Alpizar *et al.*, manuscript in preparation, 2009). Results confirm the vertical mixing of aerosols within TIC-2B systems for the particular event shown in Figure 1, and also on average during the month. The model further provides an assessment of the sulphate ratio to around 65% for aerosols inside the TIC-2B system on Figure 1, and sulphate domination in the aerosol during most of the month over the High Arctic.

[40] The cooccurrence of two phenomena does not a priori imply a causal relationship between them. In the present case, the location of the  $\text{SO}_2$  sources combined with the polar circulation can explain high sulphate concentrations in the Eastern Russia sector and eastward. Also, the absence of orographic obstacles and the presence of an ice cover (insulating from oceanic sensible and latent heat sources) limits the vertical extent of clouds in the same sectors. Nevertheless, we believe that all conditions are present for a physicochemical action of the anthropogenic aerosol, which tends to increase the ice effective radius in TIC-2B systems. We already argued that when weak cold low-pressure systems drift over the cold Arctic, thus slowly raising moisture and pollution from the boundary layer well into the midtroposphere, the SIFI may have an impact because ice supersaturation production rates remain low, so that nucleation takes place only on larger IFN. In this context, sulphuric acid (and to a lower extent ammonium sulphate) could act as a second obstacle to the onset of freezing, further limiting the competition for water vapor and allowing for the formation of larger ice particles, as in TIC-2B type. The SIFI may also be effective when active

cyclones characterized by a strong vertical velocity lift air parcels at higher altitudes, but to a lower extent. Indeed, the SIFI effect in TIC-1 fails most of the time in producing explosive growth of crystals and light precipitation, as suggested by the recurrent inability of the radar to see the small ice crystals in the upper part of the troposphere.

[41] The size discrimination for aerosol water uptake is always expected through Kelvin effect in the Köhler equation, but it is much enhanced when particles are coated with frost-inhibiting material like sulphuric acid. Eventually, acidic haze droplets can freeze, but only when sulphuric acid shell on IFN is diluted enough to allow for it. Most likely, under these conditions, the largest and most diluted haze droplets can freeze, while small droplets (at the same supersaturation) remain too acidic for freezing, thus limiting the ice crystal number concentration. If this SIFI is effective as we think, high concentrations of sulphuric acid (pollution) at the top of TIC-2B should come with large sizes of the ice crystals. This is in our opinion what the significant positive linear correlation coefficients (LCCs) between  $r_{ie}$  and  $\alpha$  reveal. However,  $\alpha$  used in the calculation does not characterize top-cloud bins, but rather bins sampled within 1.5 km above cloud tops. This methodological limitation (we do not have access to the interstitial aerosol) introduces many pairs of  $(r_{ie}, \alpha)$  values in the calculation which reduce the LCC values. Indeed, owing to the very frequent Arctic temperature inversions [Serreze *et al.*, 1992], extended aerosol layers often follow isentropic surfaces and exhibit a flat top characterized by a high vertical gradient in their concentration. Generally, cloud tops form close to aerosol layer tops, when cooling either due to adiabatic vertical motion or imbalance in the radiative budget occurs. It may happen that most IFN are not activated (if ice supersaturation remains low), in which cases we have a discernable aerosol layer exceeding the cloud top (edges), so that the index ( $\alpha$ ) may correlate positively with nearby cloud top  $r_{ie}$ . However, in many cases, when a cloud cover forms by encompassing the whole (denser) aerosol layer, aerosol concentrations just above the cloud top may not be representative of the interstitial aerosol concentrations. So, the LCC values presented in this study should be interpreted as lower limits for the “true” LCCs that exist between  $r_{ie}$  and the pollution concentrations at the top of TIC-2B covers. Extensive aircraft campaigns dedicated to the measurement of interstitial aerosol properties and ice crystal sizes would be needed for assessing the true LCCs.

[42] In sum, when comparing EBC sectors to the other Arctic sectors and to the remote Antarctic plateau, the results appear to us as a reasonable indication that high pollution concentrations favor big ice crystal populations in shallow convective systems (TIC-2B, topping in the lower troposphere) during polar nights. Subsequent effects on climate could be highest in Eastern Russia and Beaufort Sea sectors, and to a lesser extent over the Canadian Archipelago, because TIC-2B systems account for the highest proportions in the total cloud cover, and haze events are also most frequent there. Explicit numerical simulations of aerosols and clouds in some of the Arctic TIC-2B systems observed by CloudSat and CALIPSO would be useful to better understand this link. In particular, it would be interesting to evaluate if the SIFI effect cannot only favor larger crystal sizes in TIC-2B systems, but even favor their

formation, at the expense of TIC-1/2A covers. This is probably the case, since the distinction between them comes only from an arbitrary threshold fixed by the radar sensitivity (corresponding to 28–30  $\mu\text{m}$ ), and there is indeed a continuum of cases between pure TIC-2B and pure TIC-1/2A systems. The proportion of TIC-2B systems which would have developed into TIC-1/2A without the SIFI effect could in principle be estimated from the  $(r_{ie}, \alpha)$  series used for LCC calculations and an adequate relationship linking  $\Delta\alpha$  (initial change in  $\alpha$ ) to  $\Delta r_{ie}$  (consequent change in  $r_{ie}$ ).

## 5.2. Implications for the DGF Mechanism

[43] The consequences of the SIFI effect, which is in this paper not directly demonstrated but rather presented as consistent with our results, are potentially important. One direct impact could be the alteration of the radiative properties of TICs, by increasing the size of ice crystals and spreading their vertical distribution over a deep height interval, as seen in TIC-2B cases. The resulting effect would increase the atmospheric infrared cooling rate over most of the layer. On the opposite, an elevated TIC-1 warms the lower atmosphere and the surface by enhancing downward atmospheric radiation. Since TICs have a long atmospheric residence time, corresponding to the low-pressure systems lifetime (5–10 days), and act on very large horizontal scales (thousands of kilometers; see Figures 1 and 2), their direct effect on the radiation balance is likely to be very significant on the net heat balance of the Arctic during winter.

[44] Another important effect of TIC-2B and 2C types arises from the alteration of the water vapor balance associated with light precipitation, which leads to the DGF process. This effect becomes increasingly important at temperatures below  $-30^\circ\text{C}$ , for which the peak of the Planck function shifts toward the far IR and the water vapor transmittance above 17  $\mu\text{m}$  increases, opening the “dirty window” in the  $\text{H}_2\text{O}$  rotation band. Under these conditions, the atmospheric dehydration in TIC-2B systems may enhance the radiative cooling in the lower atmosphere, feeding back into dehydration to accelerate the air mass transformation. Girard *et al.* [2005] have already investigated the DGF effect in the boundary layer, and hypothesized that this could cause a surface cooling anomaly through a feedback between the diamond dust formation (TIC-2C), the water vapor greenhouse effect and cooling propagating from the surface. It is not clear at the moment if the SIFI effect can trigger such a feedback in the free lower troposphere, but new findings in this study point at a possible extension of the DGF well into the midtroposphere, with dehydration associated to TIC-2B and to acid coating on aerosols. The cooling of elevated layers greatly favors the generation of available potential energy (APE) and feeds directly in the formation of intense winter storms. It is another path for altering the atmospheric circulation at large scales.

## 5.3. Algorithm Limitations and Uncertainties

[45] Classifying remotely sensed atmospheric features is not a straightforward task, since no comprehensive method totally supported by theoretical considerations exists. From the active remote sensing to the establishment of cloud types and aerosol vertical distributions, manipulation of the information is necessary at many steps. Therefore, one must

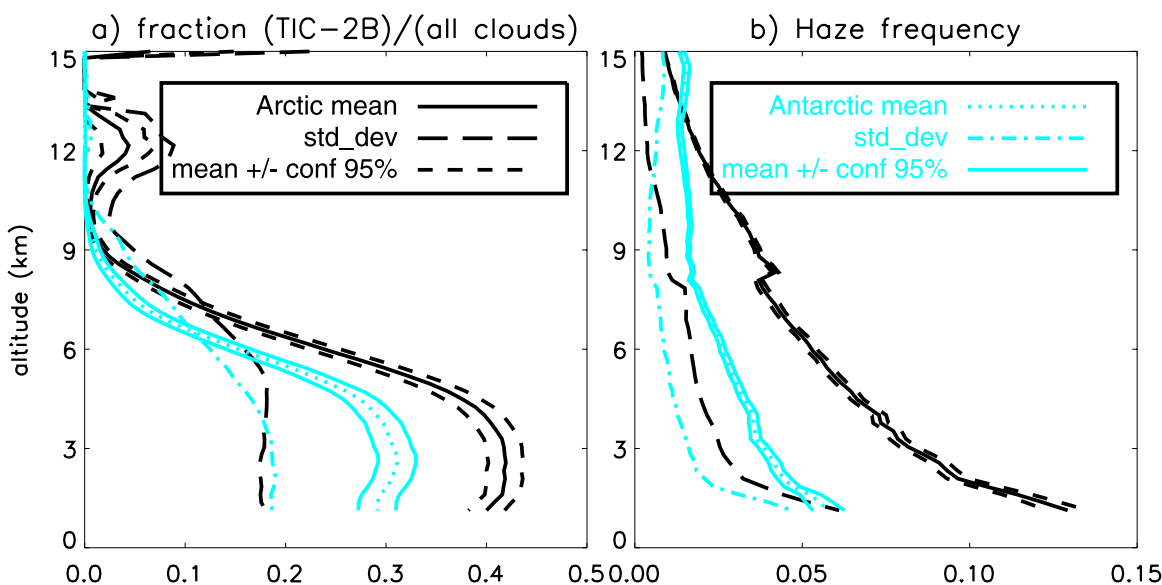


**Figure 10.** Standard deviations and 95% confidence intervals around the mean for the Arctic and Antarctic (a) fraction of TIC-2B in the cloud populations and (b) haze frequency.

assess at which extent the final products describe the true state of the polar atmospheric systems during the months investigated. Distortion of the information potentially occurs via (1) uncertainties in the lidar fields used, (2) assumptions in the radar ice water content retrieval, (3) attenuation of the lidar beam, (4) spatial and temporal mismatch in satellites orbits, (5) averaging processes, (6) feature classification algorithm assumptions and thresholds, and (7) statistical representativeness of the sampling. In this section, we discuss the nature of these uncertainty sources, and how we can cope with them.

[46] Uncertainties in the input data, due to systems technical limitations and which also encompass the retrieval algorithm assumptions in the case of the radar, could possibly modulate our main conclusions. Using noise scale factor considerations [Liu *et al.*, 2006], we estimated a geometric average random error on  $\beta_{532}$  increasing from about 19% near the surface to 29% at 8000 m for the Arctic selected scene (after degradation at the CloudSat resolution). Excluding bins with values lower than  $\beta_{532\_min} = 0.0009 \text{ km}^{-1} \text{ sr}^{-1}$  reduces the error between about 6 and 9%. The uncertainty on the  $r_{ic}$  retrieval is estimated at about 20% in the CloudSat product. A good way to assess the impact of input field uncertainties would be to make a random change of all values within their uncertainty range before performing the analysis. By repeating this operation many times, we could conclude about the robustness of our findings to input uncertainties.

[47] For our baseline algorithm, we treated attenuated input fields, and we defend the choice of not having performed a retrieval of the volume (intrinsic) backscattering by the fact that this operation requires the introduction of information which is not supported by measurements. The high variability of aerosol and water content mixtures filling sampled volumes renders arbitrary any choice for a set of optical coefficients (extinction-to-backscatter ratio, asymmetry factor, etc.) used when retrieving a volume

backscattering profile from an attenuated profile. Also, there is no guarantee that performing a retrieval of the volume backscattering prior to classifying bins would lead to more realistic results, since the choice of the multiple feature segregation thresholds would be done by considering slightly modified input scenes, so that values would be different, but still partly tuned following visual appreciation of the results produced by the algorithm. The final edges of cloud and aerosol features would possibly stay at the same place or vary only a little most of the time. A comparison of the two methods should be performed before concluding if a significant difference would be found in main conclusions, and if it were the case, only vast in situ measurement campaigns could tell if the retrieval leads to classification results closer to the reality or not.

[48] For the previously selected Arctic and Antarctic scenes, the average distance between each lidar and the closest radar sampling locations were respectively 305 and 301 m. Measurements also suffered a time lag of 10–15 s. During that period, 50 m/s winds would displace an air parcel by 500–750 m, and a 10 m/s vertical movement of water particles would translate them by 100–150 m. Considering the radar  $1.4 \times 2.5 \text{ km}$  footprint and the vertical resolution of 240 m, we think the lidar is sampling a volume comprised in the radar sampled one most of the time. Also, because of the large extension of the TIC-1 and haze layers (high profile-to-profile autocorrelation), we believe orbital mismatches do not significantly affect our conclusions.

[49] Averaging of neighboring profiles for avoiding too small signal-to-noise ratios or for comparing to the lower-resolution radar field mixes information from different volumes, and this operation may lead to feature misclassification, especially at the edge of cloud systems and near the surface. However, we see no a priori reason to think that cloud type proportions could be systematically biased.

[50] All results presented in this paper have been obtained from the same baseline algorithm, but variation of some

parameters could possibly significantly alter them. In particular, the sensitivity to the shape and parameters of the  $\delta_{\min}$  function, as well as to the  $\chi_{\min}$  and  $\beta_{532_{\min}}$  values, which together determine the segregation between TIC-1 and cloud-free bins, should be further investigated. Variations to the shape of the aerosol index function, based on  $\beta_{532}$  and  $\chi$  values, should also be performed. In addition, haze occurrence based on our cutoff at  $\alpha = 0.6$  should be compared to Arctic haze detection results based on the more conventional aerosol optical depth [Yamanouchi *et al.*, 2005]. We recognize also that several assumptions present some degree of arbitrariness, for example the method for isolating TIC-2B systems, especially when there is a gap between the radar-seen and the TIC-1 layers. Corrections could be performed for certain cloud configurations, but there will always be special cases that such an algorithm will misclassify.

[51] Owing to the great number of profiles used for this study, all differences we have emphasized are statistically significant. However, 95% confidence intervals have not been shown in figures, for clarity purpose. Figure 10 presents the vertical distribution of TIC-2B proportions (Figure 10a) and haze fraction of cloud-free bins (Figure 10b), with the standard deviations and 95% confidence intervals. For these graphs, we considered the average value for each overpass as one sampling, so that the confidence interval calculation assumes that series have 386 (Arctic) and 379 (Antarctica) values, which are weighted by the number of profiles in the scene for the averages and standard deviations calculations.

[52] Despite limitations mentioned above, we believe our baseline algorithm allows for a reasonable characterization of the polar thin ice cloud and aerosol fields, as well as for meaningful conclusions. At the same time, these limitations imply that findings remain hypothetical, and that more research is needed to support them.

#### 5.4. Further Investigation

[53] Further work includes improvement of our algorithm. This could be done by considering other TIC-1/cloud-free segregation criteria, like the layer stability and relative humidity over ice, as used notably by Ishii *et al.* [1999]. The algorithm could possibly take advantage of the characteristically low depolarization ratio of water droplets when identifying mixed-phase clouds, especially when treating next version of CALIPSO data taken with a larger off-nadir angle. For example, Intrieri *et al.* [2002] used a cutoff of  $\delta = 0.11$  for discriminating ice from liquid water content. Hu [2007] also developed a methodology for the identification of mixed-phase layers. Moreover, two-dimensional structure recognition of features could be further exploited, particularly for separating TIC-2A and TIC-2B. As mentioned previously, results sensitivity to algorithm key parameters must also be assessed.

[54] Next, our study should be extended to other winter months, for an understanding of the seasonal and interannual variation of the TIC-2B proportions and  $r_{ie} - \alpha$  correlations. The relationships between TIC types and synoptic conditions should also be further investigated.

[55] Finally, our main atmospheric inferences, especially the correlation we emphasized between the sulphate concentrations and the effective radius of ice crystals, need

more support from numerical simulations of the aerosol field and its interactions with the hydrological cycle.

## 6. Conclusion

[56] CALIPSO lidar and CloudSat radar data sets allow for a characterization of polar winter thin ice clouds and aerosols, aiming to find a relationship between high levels of pollution and the effective radius of ice particles at the top of a certain type of clouds (TIC-2B). Sampled volume bins from 386 Arctic (January 2007) and 379 Antarctic (July 2007) overpasses have been classified using an algorithm based on the CloudSat retrieved ice effective radius ( $r_{ie}$ ) and the CALIPSO backscattering at 532 nm (total and perpendicular polarization) and 1064 nm (total). Thin ice clouds of type 1 (TIC-1), seen by the lidar only because of the too small size of the ice crystals ( $<28-30 \mu\text{m}$ ), occur preferentially in the upper troposphere, and at a much higher frequency over Antarctica and Greenland–North Atlantic–Kara Sea (GNK) sectors than over Eastern Russia–Beaufort Sea–Canadian Archipelago (EBC) sectors. This difference is partly due to the absence of a high plateau (orographic lifting) and/or open-water surfaces (sensible and latent energy fluxes) over EBC sectors. TIC-2B, a radar-seen (big crystal mode) cloud type, accounts for more than 40% of the lower tropospheric clouds only over EBC sectors. The Eastern Russia and Beaufort Sea sectors also present the highest aerosol index and the highest frequency of haze occurrence. We argued that in slowly lifting TIC-2B systems, where only coarse IFN may be activated, sulphuric acid brought into the Arctic through haze events may coat and further deactivate a considerable proportion of them, favoring cloud populations made of fewer but larger ice crystals. The small but statistically significant positive linear correlation coefficients between TIC-2B top  $r_{ie}$  and the above-cloud aerosol index found in 10 of the 11 sectors support this hypothesis.

[57] Further work includes a study of the sensitivity of results to algorithm parameters and assumptions, the extension of the statistical calculations to other winter months, and the improvement of the baseline classification algorithm.

[58] **Acknowledgments.** P.G. acknowledges the Ouranos Consortium and the National Sciences and Engineering Research Council of Canada (NSERC) for financial support, as well as his Ph.D. supervision committee: Jean-Pierre Blanchet, Colin Jones, Éric Girard, and Graeme Stephens. The funding for this research was also supported by the NSERC through its International Polar Year 2007–2008 program. We also acknowledge the NASA Langley Research Center/Atmospheric Science Data Center from which CALIPSO data were obtained, and the NASA CloudSat project. Thanks finally go to the three anonymous reviewers for their valuable remarks.

## References

- Archuleta, C. M., P. J. DeMott, and S. M. Kreidenweis (2005), Ice nucleation by surrogates for atmospheric mineral dust and mineral dust/sulfate particles at cirrus temperatures, *Atmos. Chem. Phys.*, *5*, 2617–2634.
- Austin, R. T., and G. L. Stephens (2001), Retrieval of stratus cloud microphysical parameters using millimeter-wave radar and visible optical depth in preparation for CloudSat: 1. Algorithm formulation, *J. Geophys. Res.*, *106*(D22), 28,233–28,242, doi:10.1029/2000JD000293.
- Blanchet, J.-P. (1995), Mechanisms of direct and indirect climate forcing by aerosols in the Arctic region, in *Aerosol Forcing of Climate*, edited by R. J. Charlson and J. Heintzenberg, chap. 6, pp. 109–121, John Wiley, Hoboken, N. J.
- Blanchet, J.-P., and E. Girard (1994), Arctic greenhouse effect, *Nature*, *371*, 383, doi:10.1038/371383a0.

- Borys, R. D. (1989), Studies of ice nucleation by Arctic aerosols on AGASP-II, *J. Atmos. Chem.*, *9*, 169–185, doi:10.1007/BF00052831.
- Christensen, J. H. (1997), The Danish Eulerian hemispheric model—A three-dimensional air pollution model used for the Arctic, *Atmos. Environ.*, *31*, 4169–4191, doi:10.1016/S1352-2310(97)00264-1.
- Curry, J. A., W. B. Rossow, D. Randall, and J. L. Schramm (1996), Overview of Arctic cloud and radiation characteristics, *J. Clim.*, *9*, 1731–1764, doi:10.1175/1520-0442(1996)009<1731:OOACAR>2.0.CO;2.
- Eastwood, M., M. Wheeler, C. Gehrke, B. J. Murray, and A. K. Bertram (2008), Ice nucleation on and in atmospheric particles, paper presented at 235th ACS National Meeting, Am. Chem. Soc., New Orleans, La.
- Eckhardt, S., A. Stohl, S. Beirle, N. Spichtinger, P. James, C. Forster, C. Junker, T. Wagner, U. Platt, and S. G. Jennings (2003), The North Atlantic Oscillation controls air pollution transport to the Arctic, *Atmos. Chem. Phys. Discuss.*, *3*, 3222–3240.
- Girard, E., J.-P. Blanchet, and Y. Dubois (2005), Effects of arctic sulphuric acid aerosols on wintertime low-level atmospheric ice crystals, humidity and temperature at Alert, Nunavut, *Atmos. Res.*, *73*, 131–148, doi:10.1016/j.atmosres.2004.08.002.
- Gong, S. L., et al. (2003), Canadian Aerosol Module: A size-segregated simulation of atmospheric aerosol processes for climate and air quality models 1. Module development, *J. Geophys. Res.*, *108*(D1), 4007, doi:10.1029/2001JD002002.
- Hahn, C. J., S. G. Warren, and J. London (1995), The effect of moonlight on observation of cloud cover at night, and application to cloud climatology, *J. Clim.*, *8*, 1429–1446, doi:10.1175/1520-0442(1995)008<1429:TEOMOO>2.0.CO;2.
- Hostetler, C. A., Z. Liu, J. Reagan, M. Vaughan, D. Winker, M. Osborn, W. H. Hunt, K. A. Powell, and C. Trepte (2006), CALIOP algorithm theoretical basis document—Part 1: Calibration and level 1 data products, *PC-SCI-201*, NASA Langley Res. Cent., Hampton, Va. (Available at [www-calipso.larc.nasa.gov/resources/project\\_documentation.php](http://www-calipso.larc.nasa.gov/resources/project_documentation.php))
- Hu, Y. (2007), Depolarization ratio-effective lidar ratio relation: Theoretical basis for space lidar cloud phase discrimination, *Geophys. Res. Lett.*, *34*, L11812, doi:10.1029/2007GL029584.
- Intergovernmental Panel of Climate Change (2007), *Climate Change 2007: The Physical Science Basis*, 996 pp., Cambridge Univ. Press, New York.
- Intrieri, J. M., M. D. Shupe, T. Uttal, and B. J. McCarty (2002), An annual cycle of Arctic cloud characteristics observed by radar and lidar at SHEBA, *J. Geophys. Res.*, *107*(C10), 8030, doi:10.1029/2000JC000423.
- Ishii, S., T. Shibata, T. Nagai, K. Mizutani, T. Itabe, M. Hirota, T. Fujimoto, and O. Uchino (1999), Arctic haze and clouds observed by lidar during four winter seasons of 1993–1997, at Eureka, Canada, *Atmos. Environ.*, *33*, 2459–2470, doi:10.1016/S1352-2310(98)00397-5.
- Kahn, B. H., et al. (2007), Cloud type comparisons of AIRS, CloudSat, and CALIPSO cloud height and amount, *Atmos. Chem. Phys. Discuss.*, *7*, 13,915–13,958.
- Knopf, D. A., and T. Koop (2006), Heterogeneous nucleation of ice on surrogates of mineral dust, *J. Geophys. Res.*, *111*, D12201, doi:10.1029/2005JD006894.
- Liu, Y., J. R. Key, and X. Wang (2008), The influence of changes in cloud cover on recent surface temperature trends in the Arctic, *J. Clim.*, *21*, 705–715, doi:10.1175/2007JCLI1681.1.
- Liu, Z., M. Vaughan, L. Poole, C. Hostetler, and D. Winker (2002), Scene classification for the CALIPSO lidar, paper presented at International Laser Radar Conference 2002, Int. Coord. Group for Laser Atmos. Stud., Quebec City, Quebec, Canada.
- Liu, Z., W. Hunt, M. Vaughan, C. Hostetler, K. P. McGill, D. Winker, and Y. Hu (2006), Estimating random errors due to shot noise in backscatter lidar observations, *Appl. Opt.*, *45*(18), 4437–4447, doi:10.1364/AO.45.004437.
- Meyers, M. P., P. J. DeMott, and W. R. Cotton (1992), New primary ice-nucleation parameterizations in an explicit cloud model, *J. Appl. Meteorol.*, *31*, 708–721, doi:10.1175/1520-0450(1992)031<0708:NPINPI>2.0.CO;2.
- Prenni, A. J., J. Y. Harrington, M. Tjernström, P. J. DeMott, A. Avramov, C. N. Long, S. M. Kreidenweis, P. Q. Olsson, and J. Verlinde (2007), Can ice-nucleating aerosols affect Arctic seasonal climate?, *Bull. Am. Meteorol. Soc.*, *88*, 541–550, doi:10.1175/BAMS-88-4-541.
- Quinn, P. K., G. Shaw, E. Andrews, E. G. Dutton, T. Ruoho-Airola, and S. L. Gong (2007), Arctic haze: Current trends and knowledge gaps, *Tellus, Ser. B*, *59*, 99–114.
- Sassen, K. (1991), The polarization lidar technique for cloud research: A review and current assessment, *Bull. Am. Meteorol. Soc.*, *72*, 1848–1866, doi:10.1175/1520-0477(1991)072<1848:TPLTFC>2.0.CO;2.
- Schutgens, N., and D. P. Donovan (2004), Retrieval of atmospheric reflectivity profiles in case of long radar pulses, *Atmos. Res.*, *72*, 187–196, doi:10.1016/j.atmosres.2004.03.014.
- Serreze, M. C., and R. G. Barry (2005), *The Arctic Climate System*, 385 pp., Cambridge Univ. Press, New York.
- Serreze, M. C., J. D. Kahl, and R. C. Schnell (1992), Low-level temperature inversions of the Eurasian Arctic and comparisons with Soviet drifting station data, *J. Clim.*, *5*, 615–629, doi:10.1175/1520-0442(1992)005<0615:LLTIOT>2.0.CO;2.
- Sharma, S., D. Lavoué, H. Cachier, L. A. Barrie, and S. L. Gong (2004), Long-term trend of the black carbon concentrations in the Canadian Arctic, *J. Geophys. Res.*, *109*, D15203, doi:10.1029/2003JD004331.
- Shaw, G. E. (1988), Antarctic aerosols: A review, *Rev. Geophys.*, *26*(1), 89–112, doi:10.1029/RG026i001p00089.
- Sirois, A., and L. A. Barrie (1999), Arctic lower tropospheric aerosol trends and composition at Alert, Canada: 1980–1995, *J. Geophys. Res.*, *104*(D9), 11,599–11,618, doi:10.1029/1999JD900077.
- Stephens, G. L., et al. (2002), The CloudSat Mission and the A-Train: A new dimension of space-based observations of clouds and precipitation, *Bull. Am. Meteorol. Soc.*, *83*, 1771–1790, doi:10.1175/BAMS-83-12-1771.
- Vaughan, M. A., D. M. Winker, and K. A. Powell (2005), CALIOP Algorithm Theoretical Basis Document—Part 2: Feature detection and layer properties algorithms, *PC-SCI-202*, NASA Langley Res. Cent., Langley, Va. (Available at [www-calipso.larc.nasa.gov/resources/pdfs/PC-SCI-202\\_Part2\\_rev1x01.pdf](http://www-calipso.larc.nasa.gov/resources/pdfs/PC-SCI-202_Part2_rev1x01.pdf))
- Walden, V. P., S. G. Warren, and E. Tuttle (2003), Atmospheric ice crystals over the Antarctic plateau in winter, *J. Appl. Meteorol.*, *42*, 1391–1405, doi:10.1175/1520-0450(2003)042<1391:AICOTA>2.0.CO;2.
- Winker, D. M., W. H. Hunt, and M. J. McGill (2007), Initial performance assessment of CALIOP, *Geophys. Res. Lett.*, *34*, L19803, doi:10.1029/2007GL030135.
- Yamanouchi, T., et al. (2005), Arctic Study of Tropospheric Aerosol and Radiation (ASTAR) 2000: Arctic haze case study, *Tellus, Ser. B*, *57*, 141–152.

J.-P. Blanchet, P. Grenier, and R. Muñoz-Alpizar, Institut des Sciences de l'Environnement, Université du Québec à Montréal, P.O. Box 8888, Station Downtown, Montréal, QC H3C 3P8, Canada. (grenier@sca.uqam.ca)